

# Characterization, axial anisotropy and formation conditions of celestine minerals from the Jabal Eghei (Nuqay) volcanic province (southeastern edge of the Sirt Basin, southern Libya)

Pavle Tančić (✉ [pavletan@gmail.com](mailto:pavletan@gmail.com))

Geological Survey of Serbia

Maja Milošević

University of Belgrade

Darko Spahić

Geological Survey of Serbia

Bojan Kostić

University of Belgrade

Aleksandar Kremenović

University of Belgrade

Maja Poznanović-Spahić

Geological Survey of Serbia

Jovan Kovačević

Geological Survey of Serbia

---

## Research Article

**Keywords:** celestine, characterization, axial anisotropy, formation conditions, Jabal Eghei (Nuqay) volcanic province, southern Libya

**Posted Date:** July 1st, 2022

**DOI:** <https://doi.org/10.21203/rs.3.rs-1771912/v1>

**License:** © ⓘ This work is licensed under a Creative Commons Attribution 4.0 International License. [Read Full License](#)

**Additional Declarations:** No competing interests reported.

---

**Version of Record:** A version of this preprint was published at Mineralogical Magazine on November 28th, 2023. See the published version at <https://doi.org/10.1180/mgm.2023.88>.

# Abstract

Five celestine crystals, sampled from the surface at the Miocene to Pliocene Jabal Eghei (Nuqay) volcanic province (southern Libya), are characterized by applying the combination of the SEM-WDS, XRPD and IR methods; and analyzed for their color variations and minerogenesis. Three samples have greenish-blue to blue (480.4–482.5 nm), whereas the other two samples are of blue-green color (cyan; 489.1–494.1 nm). The color purity is in the 1.36–7.16 range. Their chemical composition is mutually similar, fitting into the celestine near-end members, in which exclusively 1.6–4.1 at. % of  $\text{Sr}^{2+}$  contents was substituted by  $\text{Pb}^{2+}$  (0.7–0.9 at. %),  $\text{Ba}^{2+}$  (0.5–0.7 at. %) and  $\text{Ca}^{2+}$  (0.2–0.8 at. %); including the vacancies (1.0–1.9 at. %; only in three samples). The resulting unit-cell parameters have the following ranges:  $a_0 = 8.3578(9)$ – $8.3705(6)$  Å;  $b_0 = 5.3510(5)$ – $5.3568(4)$  Å;  $c_0 = 6.8683(7)$ – $6.8767(2)$  Å and  $V_0 = 307.17(5)$ – $308.34(4)$  Å<sup>3</sup>. The XRPD and IR results are mainly in accordance with the SEM-WDS analyses, having higher mutual correlativity. However, a few discrepancies among the results are observed, further yielding several possible interpretations. The overall results show that discrepancies were primarily induced by a slight unit-cell axial anisotropy, occurring as a consequence of their thermal expansion. Essentially, the investigated Sr-bearing celestines were formed as a secondary volcanic system, emplaced over the gypsum and/or anhydrite minerals, at ~ 368–430K (~ 95–157 °C) temperature range, in the ambient pressure conditions. The study further shows that the investigated celestine minerals are likely formed at a slightly elevated temperature and pressure subsurface environment, reaching over 250 bars.

## 1. Introduction

Celestine ( $\text{SrSO}_4$ ; ideally containing 56.42% SrO and 43.58%  $\text{SO}_3$ ) is a common sulfate mineral occurring in the Earth's crust, and an important raw material often used for the production of strontium (Palache et al. 1951; Deer et al. 2013). Coupled together with anglesite ( $\text{PbSO}_4$ ), celestine belongs to the sulfates of the barite ( $\text{BaSO}_4$ ) group. These are isostructural minerals crystallizing in the orthorhombic *Pnma* (*Pbnm*) space group (N° 62). They are characterized by tetrahedral  $\text{SO}_4$  anion and cations of considerably large size ( $\text{M}=\text{Sr}^{2+}$ ,  $\text{Pb}^{2+}$  and  $\text{Ba}^{2+}$ ), the latter falling into the twelve-coordination with oxygen. The  $\text{SO}_4$  tetrahedra and  $\text{MO}_{12}$  polyhedral share own edges. Importantly, anhydrite ( $\text{CaSO}_4$ ) differs structurally (space group *Cmcm*, N° 63) from the celestine, primarily because of a relatively smaller-in-size  $\text{Ca}^{2+}$  ion, thus being excluded outside of the barite group (Hanor 2000). A statistical study on naturally-occurring celestine samples shows that the composition of the great majority is close to that of the end members, having Ba and Ca ordinarily present in the amounts ranging up to only a few at. %. In global scale, celestine occurrences are of primary sedimentary origin, diagenetic, or occurring typically as fissure and rock cavity fillings (including caves), precipitated by migrating strontium-bearing groundwater or basinal brines in carbonate rocks, concretions and nodules. In addition, celestine occurrence has often been documented in the form of hydrothermal veins and mafic volcanic rock products. Celestines have often been associated with gypsum, anhydrite, native sulfur (evaporites); strontianite, calcite, dolomite, anhydrite, gypsum, fluorite (cavities in carbonate rocks); and also occurring along with analcime, natrolite, hydroxyapophyllite, celadonite (mafic volcanoclastics). Celestine color could range from colorless to blue, to have white, yellow, orange, reddish, greenish, or brownish colors. The blue

color has often been unequally distributed in the mineral growth zones or *face loci*, whereas in some cases blue color could probably be produced by the irradiation (Palache et al. 1951; Hanor 2000; Deer et al. 2013).

Several celestine minerals of presumed sedimentary and magmatic origin are observed and collected during the Field Geological Mapping campaign of central and southern Libya (Fig. 1b). This field-mapping campaign lasted from 2005 up to 2010, carried out in the cooperation between the Industrial Research Centre (Tripoli, Libya) and the Geological Survey of Serbia (former Geoinstitute, Belgrade, Serbia).

**Fig. 1 a** The investigated area within the circum-Mediterranean realm; **b** Geological Mapping campaign of central and southern Libya (marked with green color); **c** The wider area of the Al Haruj and Jabal Eghei Volcanic Provinces; **d** Jabal Eghei Volcanic Province; and **e** The surface-exposed basalts as the result of the three Middle Miocene to Pliocene volcanic events (according to Radivojević et al. 2015). The spots of the celestine sampling locations are marked with the “x” symbol, collected from the area of the sheet NF 34-1, Geological Map of Libya, scale 1:250,000 (marked with red color)

There are four principal volcanic provinces in the Central Sahara desert, stretching from the Mediterranean coast towards the southern border of Libya: 1. Gharayan, 2. As Sawda, 3. Al Haruj Al Aswad, and 4. Jabal Nuqai or Jabal Eghei [Figure S1 in the electronic supplementary material (hereinafter ESM)]. These youngest North African (Sahara) intra-plate volcanic provinces, referred to as the Al Haruj and the Jabal Nuqay or Jabal Eghei (central and southern Libya; Fig. 1), host voluminous occurrences of near-surface celestine-bearing systems (Toljić et al. 2007; Vasić and Sheriff 2007; Toljić and Abu Agrab 2014, 2016). The investigated celestine mineral clusters are associated either with a sedimentary (*e.g.*, gypsum, anhydrite; Rundić and Daloub 2007; Vasić and Sheriff 2007; Rundić et al. 2012), or the aforementioned magmatic *i.e.*, basaltic rock assemblages (Toljić et al. 2007; Cvetković et al. 2010; Radivojević et al. 2015). The central Libyan Al Haruj volcanic system is spatially interconnected with a southern-positioned Neogene to Quaternary segment of the famous Sirt basin, and the Tibesti–Sirt arch (Rusk 2001). Spatially, the Al Haruj province of Central Libya reaches the investigated the southern-positioned Jabal Eghei Volcanic Province (Radivojević et al. 2015; Figure S1 in the ESM, #3 and #4). The occurrence of the aforementioned celestine minerals in this southern Libyan volcanic Jabal Eghei province (Fig. 1c,d,e) indicates a presence of the two mineral modes: (i) sedimentary celestine, often represented in abundant druses or clusters, occurring at the Earth’s surface (Toljić et al. 2014). Second type is (ii) magmatic celestine, often occurring as fracture-related mineral infill; and within (iii) a weathered surface crust (paleosoil). The latter is often developed between the intraplate basalt-extrusion episodes: the older (Neogene), and the youngest basalt outflows (Neogene–Quaternary) belonging the Jabal Eghei province (Radivojević et al. 2015).

The study of the Jabal Eghei Volcanic Province provides the characterization of the selected surface-exposed celestine crystals from druses or clusters (Fig. 1e and Figure S1 in the ESM, #4). The Jabal Eghei celestine minerals are characterized by applying the Scanning Electron Microscopy-Wavelength Dispersive Spectroscopy (hereinafter SEM-WDS), X-ray powder diffraction (hereinafter XRPD) and Infrared spectroscopic (hereinafter IR) methods. The study unravels chemical compositions of the sampled Jabal Eghei celestines, further characterizing the unit-cell parameters, and vibrational spectra. In addition to the applied methods, we put constraints on the celestine color variations, including the color purities. The new interpretation of Jabal Eghei celestine, provides a better insight into the axial anisotropy of the investigated crystals and their growth.

Finally, we analyzed the origin of the Jabal Eghei celestine minerals, yielding its formation temperature, and a set of other probable near-surface conditions, under which the investigated crystals were formed.

## 2. Regional Geological Setting: Al Haruj And Jabal Eghei (Nuqay) Areas

The investigated celestine-bearing area accommodates across the two major volcanic provinces in Libya: (i) Al Haruj, stretching across the central Libyan Desert, and (ii) the Jabal Eghei or Jabal Nuqay magmatic province, outcropping at the southern Libyan Desert, to the west of the Al Kufrah basin (Figure S1 in the ESM; #3 and #4). Both provinces are accommodated along the central-southern realm of the NW-SE directed Sirt basin, whereas the Jabal Eghei province reaches a segment of the African basement, referred to as the Tibesti massif (Radivojević et al. 2015).

The northern branch of the Cenozoic tectonomagmatic system corresponds to an outcropping Tertiary segment of the oil and gas-bearing Sirt Basin (Rusk 2001; Ashour et al. 2012; Figure S1 in the ESM). This Lower Cretaceous Tethyan rift system (Hallett 2002; Abadi et al. 2008; Capitanio et al. 2009) triggered the Late Cretaceous regional subsidence accommodating the formation of the Sirt basin (Cenomanian-Turonian; Rusk 2001). In terms of the oil exploration “language”, the syn-rift sedimentary loading of the newly developed accommodation space lasted from Cretaceous to Eocene, whereas the post-rift subsidence and deposition continued during Oligocene and Miocene. The latter stage is marked by the intensive subsidence and normal block faulting. The regional extension continued intermittently, lasting up to the Miocene period. The celestine sedimentary carriers are the layers outcropping as the Paleogene-Miocene sequences, distributed along the south-eastern edge of the Al Haruj Basaltic complex of central Libya (Toljić et al. 2007; Rundić and Dalub 2007; Vasić and Sherif 2007; Figure S1 in the ESM). These sequences have the best exposure along the regional escarpments, in particular, the southern Dur-at-Talah slope, located near the central massif (Fig. 1c). This escarpment is orientated perpendicular to the Al Haruj basalt plateau (Vasić and Sherif 2007; Ashour et al. 2012), exposing the layer-cake stacked Eocene–Oligocene sequences (see Ashour et al. 2012, for a discussion). The oldest sedimentary formations exposed on surface are of the Eocene age (Al Jir and Wadi Thámat formations), whereas the two overlying sequences are of the Oligocene and Lower to Middle Miocene age (Dur-at-Talah and Maradah formations; see Rundić et al. 2012, for details). The “Evaporite” Unit or Al Jir Formation (Vasić and Sherif 2007; Rundić et al. 2012) occupies the lowermost stratigraphic level, whereas the “Idam Unit”, comprises the middle portion of the escarpment. The “Sarir Unit” represents a top-sealing sequence. The Al Jir Formation contains voluminous occurrences of gypsum, and is composed of dolomite, limestone, and gypsum-bearing claystone (Rundić et al. 2012). The fibrous celestine-bearing gypsum apparently fills the bedding planes and vertical cracks, attributing the gypsum occurrence as a post-depositional feature (‘secondary gypsum’; Ashour et al. 2012). This northern central Libyan magmatic province continues into the southern-positioned investigated Jabal Eghei area (Fig. 1c,d,e).

The Jabal Eghei basaltic volcanic province is situated in the southern Libya (Fig. 1), representing an outcropping fragment of the north-western edge of the Tibesti Mts. The basalts extruded over a superposed metamorphic basement and sedimentary rocks (Toljić et al. 2014; Radivojević et al. 2015; Abdusahmin 2020). The Proterozoic basement rocks are overlain by a series composed of the Phanerozoic sedimentary and accompanying igneous rocks. The older part of this sedimentary pile is represented by the Mourizide Formation. These sediments were deposited within the Al Kufrah basin (southeastern Libya; Figure S1 in the

ESM) and consist of the Cambrian–Devonian continental deltaic and marine deposits. The younger part of the sedimentary cover belongs to the Sirt basin, its southernmost periphery. It is composed of the Paleocene–Oligocene sediments, which include the Jabal Eghei basalts. The principal structures and the configuration of the Sirt basin affected the extrusion of the basalts across both sectors, *i.e.*, the Al Haruj (Elshaafi and Gudmundsson 2016) and Jabal Eghei province (Radivojević et al. 2015). The systematic K/Ar radiometric dating of the Jabal Eghei volcanism pinpoints the Middle Miocene (~16 Ma) to mid-Pleistocene activity (<1 Ma; Radivojević et al. 2015). The three different volcanic phases are depicted: the oldest phase occurred in Middle- to Late Miocene time (basalts show K/Ar age range from  $16.1 \pm 2.9$  to  $7.9 \pm 2.3$  Ma). The second phase lasted Late Miocene to Pliocene, having the age range from  $7.19 \pm 0.36$  to  $4.32 \pm 0.35$  Ma. The youngest extrusion stage occurred from the Pliocene to the mid-Pleistocene (K/Ar radiometric ages of  $3.1 \pm 1.1$  to  $0.97 \pm 0.68$  Ma). The investigated celestine samples are mapped on top of the first volcanic extrusion phase, in the weathered crust, accommodated in the intervening position, between the second and the third basalt outflow magmatic episodes (Fig. 1e).

## 3. Materials And Methods

### 3.1. Materials

Sampling large crystals (up to 12 cm long; Fig. 2) were hand-picked during the field-mapping campaign from druses, or clusters exposed on the surface. Among these sampled crystals, five well-formed euhedral to subhedral samples are chosen, on the basis of their macroscopically visible different characteristics, *e.g.*, color, luster, transparency, shape, size and cleavage (Fig. 3).

### 3.2. Methods

The analyzed 1-5 samples do not show any radioactivity (measured *in situ* by the Saphymo-SRAT S.P.P.2 NF scintillometer, manufactured by Saphymo-PHY, Massy, France).

The electron microprobe analyses (EMPA) and back-scattered (BSE) images, were obtained on the polished sample surface, by using JEOL JSM-6610LV scanning electron microscope. This microscope is equipped with a wavelength-dispersive spectrometer (Oxford Instruments Wave 700). The operating conditions were at 30 kV accelerating potential, 10 nA beam current and 2  $\mu\text{m}$  spot size dimension. The standards used for this analytical method were natural and synthetic mineral standards, including celestine (Sr), wollastonite (Ca), barite (Ba and S) and galenite (Pb).

The XRPD measurements were conducted on a Rigaku Smartlab X-ray Diffractometer, in  $\theta$ - $\theta$  geometry (the sample in horizontal position). We used the parafocusing Bragg-Brentano geometry using D/teX Ultra 250 strip detector, in the 1D standard mode having  $\text{CuK}\alpha_{1,2}$  radiation source ( $U = 40$  kV and  $I = 30$  mA). The XRPD patterns were collected in  $5$ - $90^\circ$   $2\theta$  range, with the step of  $0.01^\circ$ , and data collection speed of  $6.15^\circ/\text{min}$ . The low background single crystal silicon sample holder is used, with the purpose to minimize the background.

The unit-cell parameters were calculated and refined using the Le Bail (1988) method. The sequence of the full-matrix least-squares fittings was refined by changing the unit-cell parameters ( $a_0$ ,  $b_0$  and  $c_0$ ), 100 parameters for the background description, Eta (p-v) parameter, parameters for the description of the halfwidths (U, V and W) and zero point; until the refinements approached convergence.

The IR spectroscopic analyses were performed by using a Perkin Elmer 597 spectrometer, by applying the KBr pellet method (2 mg of sample and 200 mg of KBr). Visible and near-infrared absorption spectrums were measured in the region 1600–200  $\text{cm}^{-1}$ .

The dominant wavenumbers of color for the raw celestine samples were measured with a diffuse reflectance apparatus (400–700 nm), by using a CCS200 spectrometer (Thorlabs). This spectrometer is equipped with the optical fiber wire, and is calculated according to the Commission Internationale de l'Eclairage (1932).

The contents of the organic matter were detected by loss of ignition at 600 °C.

## 4. Results

### 4.1. SEM-WDS study

The resulting sample SEM-WDS analyses chemistry is homogeneous, and reveals no Sr, Ca, Ba, Pb or S zoning within the samples, and various mineral phases (Figure S2 in the ESM and Table 1). The results show a similar chemical content among the analyzed samples. The major SrO and  $\text{SO}_3$  contents are in the range of 54.33-55.21 ( $\Delta_{\text{SrO}}=0.88$ ) and 43.23-43.93 ( $\Delta_{\text{SO}_3}=0.70$ ) wt. %, respectively. Among the minor oxides, PbO, BaO and CaO are in the range of 0.87-1.04 ( $\Delta_{\text{PbO}}=0.17$ ), 0.42-0.62 ( $\Delta_{\text{BaO}}=0.20$ ) and 0.07-0.24 ( $\Delta_{\text{CaO}}=0.17$ ) wt. %, respectively. These are adequate to the major celestine minerals with a minor anglesite, barite and anhydrite substituted components.

According to the calculated apfu's (Table 1), it was observed that the samples 1 and 4 show ideal (or almost ideal) stoichiometry, between M and S ions; including the crystal chemical formulas of  $(\text{Sr}_{0.984}\text{Pb}_{0.009}\text{Ba}_{0.005}\text{Ca}_{0.002})\text{SO}_4$  and  $(\text{Sr}_{0.978}\text{Pb}_{0.008}\text{Ca}_{0.008}\text{Ba}_{0.007})_{1.001}\text{SO}_4$ , respectively. On the other hand, samples 2, 3 and 5 show a minor non-stoichiometry, having a small deficit of M cations of *ca.* 1, 1 and 2 at. %, respectively. Accounting that the sulphur content shows a slight excess from the value of 1, we preliminarily suppose that such deficits were induced by a tentative presence of the sum of the total (hereinafter X):  $\text{H}^+$  and/or  $(\text{H}_3\text{O})^+$  and/or  $\text{OH}^-$  (from  $\text{H}_2\text{O}$ ); and/or vacancies. These, for example, could not be depicted accounting the limitations of the WDS method. Accordingly, the crystal chemical formulas of the samples 2, 3 and 5 could be presented as:  $(\text{Sr}_{0.970}\text{X}_{0.010}\text{Pb}_{0.008}\text{Ba}_{0.007}\text{Ca}_{0.005})\text{S}_{1.003}\text{O}_4$ ,  $(\text{Sr}_{0.973}\text{X}_{0.010}\text{Pb}_{0.007}\text{Ba}_{0.005}\text{Ca}_{0.005})\text{S}_{1.003}\text{O}_4$  and  $(\text{Sr}_{0.959}\text{X}_{0.019}\text{Pb}_{0.008}\text{Ba}_{0.007}\text{Ca}_{0.007})\text{S}_{1.006}\text{O}_4$ , respectively. Hence, it could be concluded that all of the studied samples are quite similar among each other and suite to the celestine near-end members, in which exclusively 1.6-4.1 at. % of  $\text{Sr}^{2+}$  content ( $\Delta_{\text{Sr}}=2.5$  at. %) is substituted by  $\text{Pb}^{2+}$  (0.7-0.9 at. %),  $\text{Ba}^{2+}$  (0.5-0.7 at. %),  $\text{Ca}^{2+}$  (0.2-0.8 at. %), and the X (1.0-1.9 at. %; in three samples) component. The apfu content of Sr, between the samples, shows an increase of  $5 < 2 < 3 < 4 < 1$ , whereas the ratios of the  $\Sigma(\text{Pb}+\text{Ba})/\Sigma(\text{Ca}+\text{X})$  increase according  $5 < 3 < 2 < 4 < 1$ .

By using the apfu's 12-coordinated  $M^{2+}$  cations, *i.e.*,  $Ca^{2+}$ ,  $Sr^{2+}$ ,  $Pb^{2+}$  and  $Ba^{2+}$  derived from the WDS results (Table 1) and their ionic radiuses ( $r_M$ ) of 1.34Å, 1.44Å, 1.49Å and 1.61Å, respectively (Shannon, 1976), we have calculated the theoretical ionic radiuses of these cations (Table 2). The results show that the calculated occupancies of the twelve-coordination site are as expected, being also mutually quite similar, further attesting the previously suggested similarities among the analyzed samples ( $\Delta_{occ}=1.99$  at. %). This further includes the deficit of the M cations of about 1, 1 and 2 at. % at samples 2, 3 and 5, respectively. In this case, the increase is in a slightly different order of  $5<3<2<1<4$ .

## 4.2. XRPD study

The XRPD patterns [Figure S3 (column I) and Table S1 in the ESM] show that the observed inter-planar spacings ( $d_{obs}$ ) are very similar across the investigated samples, and also are in line with the celestine ICDD-PDF's 89-0953 (Burger et al. 1998) and 05-0593 (Swanson and Fuyat 1953) reference standards. Because there are no other minerals detected, these samples should be interpreted exclusively as the monomineral phases, corroborating the SEM-WDS results. On the contrary, the observed intensities ( $I_{obs}$ ) show a remarkable difference relative to the applied standards. For example, the strongest standards reflection ( $hkl$  211) are with the relative intensity ratios (hereinafter RIR), reaching solemnly up to only 25 % (sample 1). In addition, a comparative presentation of the reflections with various Miller's  $hkl$  indices showing significant variety in the correlations between the analyzed samples (Figure S4 in the ESM). Namely, samples 3 and 5 show a clearly visible higher RIR's directed towards the axis  $c_0$ , *i.e.*, the  $[00]$  direction ( $hkl$ 's: 002, 004 and 006; Figure S4a,g,j in the ESM). The rest of the reflections, *i.e.* the samples 1, 2 and 4 have a higher RIR's (Table S1 in the ESM). On the other hand, the samples 2 and 4 show a less prominent trend, yet sufficiently visible inclining towards the axis  $b_0$ , *i.e.*,  $[0k0]$  direction ( $hkl$ 's: 020 and 040; Figures S4e right and S4i left in the ESM) and towards the  $hkl$  323 (Figure S4h in the ESM), as well. Such differences could be induced by the preferred orientation, accounting a variety in the cleavage properties (*i.e.* {001} perfect, {210} good and {010} poor; Palache et al. 1951; Deer et al. 2013). The difference could be also induced by the structural variation(s), which will be analyzed later.

By using the equation of Goldish (1989), we have calculated the content of the substituted  $SrSO_4$  mole fractions (Table 3). Taking into account that this equation is valid for the barite-celestine solid solution (and hence obtained results should be treated cautiously), we tentatively presumed that from 0.2 (samples 1 and 5) to 2.4 (sample 4) mole fractions of  $SrSO_4$ , were replaced by  $BaSO_4$ . However, due the fact that  $Pb^{2+}$  cation (Table 1) has slightly larger values than  $Sr^{2+}$ , yet smaller than  $Ba^{2+}$  (Shannon, 1976), these molar substitutions of  $SrSO_4$  should have a something larger content. On the other hand, from 0.2 (sample 3) to 0.6 mol. % (sample 2) of  $SrSO_4$  could be substituted by a smaller one (such as  $CaSO_4$ , for example) or caused by the vacancies at the M site. Accordingly, the maximal difference of the  $SrSO_4$  content among the investigated samples is about 3 mol. %, having the substitutions that are increasing in the following order:  $2<3<1=5<4$ .

The unit-cell parameters were calculated and refined by using the Le Bail profile fitting method [Figures S3 (column II) and S5; and Table S2 in the ESM], and presented in Table 4. As it was expected from the observed inter-planar spacings ( $d_{obs}$ , Table S1 in the ESM), all of the calculated unit-cell parameters are quite similar

between the investigated samples, fitting additionally into the reference data standards. However, it could be indicative that different-type variations between the samples are documented. Namely, the  $a_0$  and  $c_0$  axes show  $2 < 3 < 5 < 1 < 4$ , for the volume  $V_0$  it is  $2 < 3 < 1 \sim 5 < 4$ , whereas for the  $b_0$  axis has  $2 < 1 < 3 \sim 5 < 4$  variations.

With regards the mutual correlations between the unit-cell dimensions (and for all further, as well) variations, the following statistical data are calculated with the MS Excel program, *i.e.* coefficients of the regression- $R^2$  (hereinafter correlations-C). These correlations, reported in our previous studies of bauxites and some other sulfate minerals (Cvetković and Tančić 2019; Tančić et al. 2021) have proven themselves to be a very useful accessory tool, allowing comparison between various parameters. According to the results, the polynomial variations between the  $a_0$ ,  $c_0$  and  $V_0$  parameters are slightly better than the linear (Figure S6 in the ESM), suggesting the deviations from Vegard's law, which is in concordance with results of Goldish (1989) and Antao (2012). A very high positive correlations C(1) are associated with the  $a_0$  by  $c_0$ ;  $a_0$  by  $V_0$ ; and  $c_0$  by  $V_0$  parameters of 0.999; 0.985; and 0.990; respectively. The variations of  $b_0$  axis by  $a_0$ ,  $c_0$  and  $V_0$  parameters (Figure S7 in the ESM) show slightly lower, yet also very high positive correlations C(2) of 0.880; 0.951; and 0.956; respectively. The positions of the polynomial variations of the investigated samples (Figures S6 and S7 in the ESM) with regards to the celestine, anglesite and barite reference standards (ICDD-PDF's: 89-0953, 36-1461 and 24-1035, respectively) are also outlined (Figure S8 in the ESM). A lower C(2) correlativity for the variations, may be significant, accounting the relationship with the larger angle declinations, documented between the celestine-anglesite and the celestine-barite solid-solutions joins (Figure S8a,c,e in the ESM). Such differently angled declinations were obviously induced by a different expansion behavior of the unit-cell parameters, ranging between the  $Sr^{2+}$ - $Pb^{2+}$ ,  $Sr^{2+}$ - $Ba^{2+}$  and  $Pb^{2+}$ - $Ba^{2+}$  substitutions, *i.e.*, between the various solid-solutions series. Namely, the calculated differences in this study (Table S3 in the ESM) show that a highest expansion behavior is among the  $a_0$  and  $c_0$  axes and the volume  $V_0$ . On the other hand, different substitutions do not significantly affect the  $b_0$  axis.

## 4.3. IR study

The major vibrational areas are in the regions between 435-475, 602-650, 995-1005, 1080-1192 and 1200-1248  $cm^{-1}$  (Figure S9 in the ESM and Table 5). Two broad bands are observed across all of the investigated samples in the region between 435 and 475  $cm^{-1}$  and they are more pronounced in samples 1 and 2, respectively to the other samples. The vibrational band that is on 613-614  $cm^{-1}$  is highly pronounced in the samples 1 and 2, whereas its position in the sample 3 is slightly shifted towards 608  $cm^{-1}$ . The biggest shift is observed in the samples 4 and 5, having the band peak at 602 and 604  $cm^{-1}$ , respectively. A smaller doublet is visible between 610 and 622  $cm^{-1}$ . This doublet is observed on the 622  $cm^{-1}$  for the samples 1 and 2, it is shifted to 612  $cm^{-1}$  in the sample 3, whereas in the samples 4 and 5 it is observed on the 609 and 610  $cm^{-1}$ , respectively. The vibrational features in the region 995-1005  $cm^{-1}$  are more pronounced in the samples 1 and 2, once compared to the rest of the investigated samples. The region between 1080 and 1248  $cm^{-1}$  is a complex group of bands, wherein some of them have the form of a doublet band.

Minerals from the barite group are isostructural, resulting in a vibrational spectra that are mutually similar, whereas additional spectral features have the form of a small offset. The latter are the result of different associated cations in the structure (Lane 2007). The internal vibrational features present in solid-state sulfates, appear at around 1050-1250 ( $\nu_3$ ),  $\sim 1000$  ( $\nu_1$ ),  $\sim 500$ -700 ( $\nu_4$ ), and  $\sim 400$ -500 ( $\nu_2$ )  $\text{cm}^{-1}$ . These are occurring as a result of asymmetric and symmetric stretching and bending of the  $\text{SO}_4$  anion (Herzberg 1945; Nakamoto 1986; Vassallo and Finnie 1992; Bishop and Murad 2005; Lane 2007), including the lattice vibrations at around  $550 \text{ cm}^{-1}$  and less (Serna et al. 1986; Clark 1999; Lane 2007). The  $\nu_1$  band is known to be significantly stronger and more pronounced than the  $\nu_2$  band which is usually not observable in the infrared spectra of sulfates (Hezel and Ross 1966; Lane 2007). Lane (2007) reported that a single  $\nu_2$  band at  $471 \text{ cm}^{-1}$  is visible in the spectrum of celestine, whereas Ross (1972, 1974) observed this band at *ca.*  $491 \text{ cm}^{-1}$ . As reported by Ross (1974) and Moenke (1962), the  $\nu_2$  bands are identified at  $\sim 465$  and  $\sim 420 \text{ cm}^{-1}$  within the transmission spectrum. According to Lane (2007), the spectral features for the Sr as a major element in celestine, are evident at  $1238$  and  $1138 \text{ cm}^{-1}$  for  $\nu_3$ . The  $\nu_4$  band is evident on  $648$  and  $614 \text{ cm}^{-1}$ , whereas on  $991 \text{ cm}^{-1}$ , the  $\nu_1$  band is observable. Moenke (1956) reports that the deformations of the  $\text{SO}_4$  tetrahedra in the optically uniaxial sulfates occur as a doublet on  $620$  and  $1150 \text{ cm}^{-1}$  bands. The isomorphous substitution of Sr and Ba typically occurs in the series of barite group of minerals, in particular between celestine and barite, although celestine may contain a limited amount of  $\text{Ca}^{2+}$  (Bernstein 1979).

Considering that  $\text{Ca}^{2+}$  ion is almost of the same size as  $\text{Na}^+$ , we also take into consideration that a substitution between these two ions may also have been occurring. The hypothesis is that  $\text{K}^+$  ions have a higher likelihood to replace  $\text{Sr}^{2+}$  in the structure, than the  $\text{Na}^+$  that in turn has a similar ion radius to  $\text{K}^+$  ion. As a result, the charge imbalance from this substitution could be compensated with the additional  $\text{Na}^+$  or  $\text{H}^+$  substitutions (Bernstein 1979). The WDS analyses of the investigated samples (Table 1) shows that the contents of  $\text{K}_2\text{O}$  and  $\text{Na}_2\text{O}$  are below the detection limit, indicating that these elements are not present in the substitutional positions in the structure. However,  $\text{PbO}$ ,  $\text{BaO}$  and  $\text{CaO}$  are present in a considerable amount. The vibrational features of Ba have a slight offset towards the Sr vibration bands, and are documented on  $1220$ ,  $1128$  ( $\nu_3$ );  $641$ ,  $611$  ( $\nu_4$ );  $981 \text{ cm}^{-1}$  ( $\nu_1$ ) (Lane 2007). The shift of the high-frequency position of the  $\nu_3$  fundamental bands is documented in the sulfate series with  $\text{Ca}^{2+}$ , in which the  $\nu_3$  band occurs at a lower-frequency (lower wavenumber) position (Lane 2007). The spectral features of  $\nu_3$ ,  $\nu_4$ , and  $\nu_1$ , are systematically offset to smaller wavenumbers for the sulfates containing Pb ( $\nu_3 = 1183$ ,  $1054$ ;  $\nu_4 = 632$ ,  $598$ ;  $\nu_1 = 960 \text{ cm}^{-1}$ ) sulfates (Lane 2007). The results are highly correlative with the rest of the applied methods, in particular the SEM-WDS and XRPD, indicating that the samples are of a monomineral composition.

## 4.4. Color study

Considering the purity of the color observed in the celestine samples, and the fact that color represents the saturation or its shade, the samples 1, 2 and 4 exhibit several nuances ranging between  $480$  and  $482 \text{ nm}$  (Table 6). This corresponds to greenish-blue to blue color, *i.e.* between  $492$  and  $455 \text{ nm}$ . Due to the color purity, these shades are close to the purest white (Figure S10 in the ESM). On the other hand, samples 3 and 5 exhibit a dominant wavenumber in the range that corresponds to blue-green (cyan) color. The sample 3 has the

lightest shade of color (Table 6), nearest to pure white, represented with the illuminator. The sample 5 has the most intense color shade, with the purity of the color that is farthest from the pure white, once compared to the rest of the celestine samples (see Figure S10 in the ESM).

The color centers of the functional groups, such as  $\text{SO}_4^-$ ,  $\text{SO}_3^-$ ,  $\text{SO}_2^-$  and  $\text{O}^-$  show absorption in the visible light area, which effectively leads to the production of the blue color of the samples (Bernstein 1979). Nevertheless, this blue color can also be influenced by an eventual presence of organic inclusions (Stromeyer 1821), inclusions of additional minerals such as vivianite, colloidal gold or sulfur (Wittstein 1856; Doelter 1915; Friend and Allchin 1939, 1940). The blue color can also be affected by the charge transfer between the elements in the structure, and/or their substitutions (Schulman and Compton 1962; Bershov and Marfunin 1967; Isetti 1970; Bernstein 1979). The chemical analyses of the celestine samples (Table 1), show that the content of gold is under the detection limits, fitting with the Bernstein (1979) report, which explains that the blue color, in this case, cannot be influenced by the colloidal gold-theory, or to be correlative with the content of Fe or Na in the samples (which are also under the detection limit). We underline, that no additional inclusions of minerals were detected by this study, thus excluding this theory as well. The difference of the formation temperatures, indicate that the color is influenced by the color centers; however, there is no uniform association between them. With exception of the color centers of the functional groups, there is a correlation with the highest contents of Ca and the organic matter, exclusively in the sample 4 (Tables 1 and 6), leading towards a deepest blue shade.

## 5. Discussion

### 5.1. Disagreements between the WDS and the XRPD results

It is indicative that there are a few determined discrepancies between the WDS and the XRPD results (Tables 1-4). Namely, accounting the different variation trends between the samples, samples 3 and 5 have changed the place with the sample 2 ( $5 < 3 < 2 < 1 < 4$  vs.  $2 < 3 < 5 < 1 < 4$ ; Tables 2 and 4), whereas sample 1 have changed own position just in a few places, belonging the sample 4 ( $5 < 2 < 3 < 4 < 1$  (apfu contents of Sr) and  $5 < 3 < 2 < 4 < 1$  [ratios  $\Sigma(\text{Pb}+\text{Ba})/\Sigma(\text{Ca}+\text{X})$ ] vs.  $2 < 3 < 5 < 1 < 4$ ; Tables 1 and 4). Thus, there is a poor correlation C(3) of the ionic radiuses (Table 2) variations by the  $a_0$ ,  $b_0$ ,  $c_0$  and  $V_0$  unit-cell parameters (Table 4) of 0.731; 0.366; 0.620 and 0.593, respectively (Figure S11 in the ESM). Optionally, the interpretation of these disagreements could be reached by assessing the likely structural or/and compositional circumstances, such as: (i) inadequate structural model, leading to the poorly calculated unit-cell parameters; or/and (ii) a wrong apfu's basis, leading to the miscalculation of the crystal-chemical formulas, and the corresponding ionic radiuses; or/and (iii) the presence of other previously undetected mineral phases, leading also to the miscalculation of the crystal-chemical formulas, and the corresponding ionic radiuses; or/and (iv) the incomplete calculation of the ionic radiuses; or/and (v) that the palette of the structural variations within the samples could take place. Despite seemingly perplexing or even (in)significant, we believe that the listing of these possible reasons could be of highest importance, as a step towards avoiding any eventual misleading. Hence, neither of these disagreements will be *a priori* rejected, and disagreements will be further investigated in a great detail.

(i) The study emphasizes the Le Bail (1988) method, because of the extensive experiments previously applied for the barite-group of minerals (Kuang et al. 2017; Li et al. 2018; Girard et al. 2019; Ye et al. 2019). Very good profile parameters and relatively low reliability factors characterized by this method (Table S2 in the ESM), satisfactory level of quality of the obtained difference plots [Figures S3 (column II) and S5 in the ESM], and a very high positive correlations C(1) and C(2) among the unit-cell parameters (Figures S6 and S7 in the ESM), corroborate that the studied samples are suitable to celestines and its structural model. A lower quality result of the samples 3 and 5, are most probably influenced by their higher preferred orientations, in comparison with the samples 1, 2 and 4 (see Table S1 and Figure S4 in the ESM). In addition, a considerably lower esd's (Table 4), which are mostly better even than the reference standards used, provide the validation that the unit-cell parameters were well-calculated and refined. Therefore, these facts allow us to reject this as a possible reason for the aforementioned disagreements.

(ii) In this study, we calculated the apfu's by using the 4 oxygen anions (Table 1), what led to the calculated theoretical ionic radiuses of the M cations (Table 2). Another choice is that the apfu's could be also calculated at the 2 ( $\Sigma M+S$ ) ions basis. For example, Antao (2012) for therein studied celestine derived  $(\text{Sr}_{0.966}\text{Fe}_{0.001}\text{Ba}_{0.001})_{0.968}(\text{SO}_4)_{1.027}$  chemical formula, which is adequate to the herein calculated  $(\text{Sr}_{0.953}\text{Fe}_{0.001}\text{Ba}_{0.001})_{0.955}\text{S}_{1.016}\text{O}_4$  (F and Cl apfu's in both cases remained the same, *i.e.* 0.002 and 0.004, respectively; Table S4 in the ESM). As expected, there are no significant differences for the samples 1 and 4; whereas the samples 2, 3 and 5, show a slightly higher content of Sr, S and O ions. The results show that the samples are mutually similar, fitting into the celestine near-end members having only 1.6-3.5 at. % of  $\text{Sr}^{2+}$  content ( $\Delta_{\text{Sr}}=1.9$  at. %), substituted by the same contents of  $\text{Pb}^{2+}$  (0.7-0.9 at. %),  $\text{Ba}^{2+}$  (0.5-0.7 at. %) and  $\text{Ca}^{2+}$  (0.2-0.8 at. %). The variations of the apfu content of the Sr and  $\Sigma(\text{Pb}+\text{Ba})/\Sigma(\text{Ca}+\text{X})$  ratios remained identical, *i.e.*,  $5 < 2 < 3 < 4 < 1$  and  $5 < 3 < 2 < 4 < 1$ , respectively. The only difference is a slightly lower content of the X component (0.7-1.3 at. %;  $\Delta_{\text{X}}=0.3-0.6$  at. %) which, in turn, lead to a slightly higher calculated ionic radiuses for the aforementioned three samples, and their  $5 < 3 < 2 < 4 < 1$  variation (Table S5 in the ESM). However, the resulting correlations C(4), among these ionic radiuses variations by the  $a_0$ ,  $b_0$ ,  $c_0$  and  $V_0$  parameters (Table 4) having 0.611; 0.254; 0.501 and 0.467, respectively (Figure S12 in the ESM), are significantly less-correlative than the previous one [*i.e.* C(3); Figure S11 in the ESM]. Such a low correlativity allows rejecting of this possibility as well.

(iii) Although the observed chemical composition is rather simple (Table 1), the X component could hypothetically indicate to the presence of other mineral phases, such as gypsum ( $\text{CaSO}_4 \times 2\text{H}_2\text{O}$ ), anhydrite ( $\text{CaSO}_4$ ), native sulfur (S) and calcite ( $\text{CaCO}_3$ ). It is well known that these mineral phases have often been occurring in the paragenesis with celestine (Palache et al. 1951; Deer et al. 2013). In addition, there is a possibility of the presence of numerous other minerals, such as anglesite, barite, strontianite ( $\text{SrCO}_3$ ), aragonite ( $\text{CaCO}_3$ ), cerussite ( $\text{PbCO}_3$ ), hydrocerussite [ $\text{Pb}_3(\text{CO}_3)_2(\text{OH})_2$ ], witherite ( $\text{BaCO}_3$ ),  $\text{SrSO}_4 \times 1/2\text{H}_2\text{O}$  phase (Takahashi et al., 1993) etc., making the interpretation even more complex. In order to check an eventual presence of anhydrite (samples 1 and 4) and gypsum, including other minerals with the X component (samples 2, 3 and 5), we implemented the additional recalculations of the WDS analyses (Table S6 in the ESM). These recalculations are based on the CaO component, the apfu's deficit of the M cations; including the sulfur excess (Table 1).

According to the results, it could be speculated that there is a tentative minor content of: a) anhydrite in the samples 1 (0.17 mol. %) and 4 (0.58 mol. %); b) gypsum in the samples 2 (0.49 mol. %), 3 (0.46 mol. %), and 5 (0.68 mol. %); and c) other minerals with the X component in the samples 2 (0.10 mol. %), 3 (0.30 mol. %), and 5 (0.60 mol. %). If these contents are taken into the account, it appears quite logical and understandable that these minerals couldn't be detected by the XRPD method, because of their quantity that is below the detection limit of about 1-2 mol. This includes a close inspection of the  $2\theta$  angle regions, which are fitting into the strongest reflections for these phases, as well. In addition, the WDS method could fail to separate these from the celestine, mainly because of the similarities in the chemical composition, and its limitations of detecting some elements (already mentioned before). The apfu's calculation of 12-coordinated  $M^{2+}$  cations (Table S6 in the ESM) was moreover recalculated by applying the theoretical ionic radiuses of these cations (Table S7 in the ESM). The new correlations C(5) of such ionic radiuses by the  $a_0$ ,  $b_0$ ,  $c_0$  and  $V_0$  parameters of 0.927; 0.620; 0.850 and 0.832, respectively (Figure S13 in the ESM) have a considerably better fit than the C(3) (Figure S11 in the ESM). Consequently, a minor content of anhydrite and/or gypsum could be present together with the investigated celestines. In contrast, the presence of other minerals with the X component in the paragenesis with celestine (although with the desired  $2 < 3 < 5 < 1 < 4$  variations) should be rejected, accounting their lower correlativity [C(6)] of 0.653; 0.325; 0.526 and 0.516, respectively (Figure S14 in the ESM) in comparison with the previously considered two options [*i.e.* C(3) and C(5); Figures S11 and S13 in the ESM].

The results show that the majority of the samples are represented with celestine, having a neglected anhydrite or gypsum content (0.17-0.68 mol. %). The investigated celestines have the form of solid solutions, with a low quantity of anglesite and barite. The presence of the vacancies (hereinafter Z), and the excessive sulfur content in the samples 2, 3 and 5 are also documented. Therefore, exclusively 1.4-3.2 at. % of the  $Sr^{2+}$  content ( $\Delta_{Sr}=1.8$  at. %) was substituted by the  $Pb^{2+}$  (0.7-0.9 at. %),  $Ba^{2+}$  (0.5-0.7 at. %), including Z (0.8-1.7 at. %; in three samples). Thus, the new, recalculated crystal-chemical formulas are:  $(Sr_{0.986}Pb_{0.009}Ba_{0.005})SO_4$  (sample 1),  $(Sr_{0.977}Z_{0.008}Pb_{0.008}Ba_{0.007})S_{1.002}O_4$  (sample 2),  $(Sr_{0.979}Z_{0.009}Pb_{0.007}Ba_{0.005})S_{1.003}O_4$  (sample 3),  $(Sr_{0.985}Pb_{0.008}Ba_{0.007})SO_4$  (sample 4) and  $(Sr_{0.968}Z_{0.017}Pb_{0.008}Ba_{0.007})S_{1.006}O_4$  (sample 5). The apfu content of the Sr in all of the samples remain the same as for those exhibited in Table 1, *i.e.*, they increase as  $5 < 2 < 3 < 4 < 1$ .

Finally, the recalculated occupancies (calc<sup>1,2</sup>; Table S7 in the ESM) of the twelve-coordination site have very similar values, corroborating the similarities among the samples ( $\Delta_{occ}=1.70$  at. %), moreover, having the increase in the same order ( $5 < 3 < 2 < 1 < 4$ ; Table 2). However, despite this option of the dominant celestines with the presence of a lower amount of gypsum and anhydrite fits better than that of the monomineral celestines (and because of that it could be eventually accepted), its correlation is quite far from the ideal case. Therefore, this option does not provide a complete explanation of the previously discussed discrepancies and their link with the XRPD results, thus being of tentative character.

(iv) According to the apfu's deficit of the M cations in the samples 2, 3 and 5 (Table 1), it could be speculated that the theoretical ionic radiuses need another recalculation, this time by adding the appropriate sulfur excess of 0.3, 0.3, including 0.6 at. % of the  $S^{6+}$  taken from the tetrahedral site (0.12 Å in coordination IV; Shannon, 1976), respectively. The two options are chosen (Table S8 in the ESM) as the (1) monomineral celestines (Table 2) and the (2) major celestines, barely having any anhydrite or gypsum (Table S7 in the

ESM). A similar correlation of these ionic radii by the  $a_0$ ,  $b_0$ ,  $c_0$  and  $V_0$  parameters of 0.733; 0.368; 0.622 and 0.595, respectively [C(7); Figure S15 in the ESM]; including these of 0.669; 0.300; 0.558 and 0.525, respectively [C(8); Figure S16 in the ESM] is observed in these two cases. However, neither the first, nor the second option do not reach any improvement, in regards to those from the C(3) (Figure S11 in the ESM). Hence, this correlation should also be rejected as a possible reason for the aforementioned disagreements. At last, a single remaining solution should be taken into consideration.

(v) Although the crystal structure refinements are beyond the scope of this paper, our previous studies of various mineral species, and solid-solutions, have demonstrated that the different unit-cell parameters, various polyhedral distortions, site occupancy factors, bond lengths, bond angles, valence units, etc., could be induced either by (a) the different inserted cations into the mineral structure; or/and by (b) the different conditions of their formation, in particular, the temperature and pressure (Tančić 2017, 2018; Tančić and Kremenović 2022; Tančić et al. 2012, 2020).

(a) Whilst considering the influenced variations of the unit-cell parameters accounting the different inserted cations into the mineral structure, we initiated the process, by introducing the calculations of their presumed values by the multiplication of the Sr, Ca, Pb and Ba apfu's with the corresponding unit-cell parameters of celestine, anhydrite, anglesite and barite reference standards (ICDD-PDF's: 89-0953, 37-1496, 36-1461 and 24-1035, respectively). For the selected apfu's, we have chosen the two previously discussed options: (1) the celestines as the monomineral phases (Table 1); and (2) the option of the celestines without Ca, which hypothetically belongs to the minor amounts of gypsum and anhydrite phases (Table S6 in the ESM). The results (presented at Table S9 in the ESM) indicate that the largest differences ( $\Delta$ ) between these presumed values and those of the XRPD method (Table 4) are, valid for both options, occurring in the samples 2, 3 and 5. Such correlativity is expected and suites to the already emphasized vacancies, and the here used calculations. Accordingly, the ratios increased by ca. 1, 1 and 2 %, respectively. In both cases, we observe an excellent correlations of the calculated ionic radii (Table 2 and Table S7 in the ESM) by the  $a_0$ ,  $b_0$ ,  $c_0$  and  $V_0$  parameters: (1) 1.000; 1.000; 1.000 and 0.995, respectively [C(9); Figure S17 in the ESM]; and (2) 0.997; 0.998; 0.997 and 0.977, respectively [C(10); Figure S18 in the ESM]. Because both options are almost identical, this couldn't be used as a reliable parameter for distinguished factors among them. On the other hand, these results further indicate that the presumed unit-cell parameters should be theoretically near the realistic chemical composition. However, as discussed earlier, such scenario is obviously not the case. Namely, the presumed unit-cell volumes of the samples 2, 3 and 5 have no fitting in no case, because they have significantly lower values, even by comparing with the anhydrite (ICDD-PDF: 37-1496;  $V=305.60 \text{ \AA}^3$ ) reference standard. Consequently, we observe a very poor correlation between the presumed (Table S9 in the ESM) and determined (Table 4)  $a_0$ ,  $b_0$ ,  $c_0$  and  $V_0$  unit-cell parameters of 0.397; 0.388; 0.403 and 0.348, respectively [C(11); Figure S19 in the ESM].

Thus, we further reconsider the impact of the existing vacancies in the celestine structure on their unit-cell parameters. Namely, the available reference data (Table S10 in the ESM) show that there is an example having a significant content of the vacancy of 3 at. % [Antao 2012; already discussed within part (ii)]. This celestine example has more-less similar [ICDD-PDF's: 05-0593 and 89-0953; Table 4; Miyake et al. (1978)], or even larger unit-cell parameters, relative to those without any vacancy [Hawthorne and Ferguson (1975);

Jacobsen et al. (1998); Ye et al. (2019)]. Furthermore, three selected samples showing the identical average  $\langle M-O \rangle$  distances of 2.827(1) Å (Hawthorne and Ferguson 1975; Jacobsen et al. 1998; Antao 2012). Accordingly, it seems that the existing vacancies in the celestine structure do not have any significant impact on their unit-cell parameters. The reasons for such behavior could be the geometrical changes of the  $SO_4$  and  $MO_{12}$  polyhedral, *i.e.*, a decrease of the average  $\langle M-O \rangle$  distance, the charge on the O ions that have lower values, including the average  $\langle S-O \rangle$  distance that is longer in this case; or *vice versa* (Antao 2012). In addition, the tetrahedral distortions are a function of the geometry of the structure, rather than the chemistry of the twelve-coordinated site (Hawthorne and Ferguson 1975; Brigatti et al. 1997). In order to check the afore described option, another two variances discussed earlier (ii-iv) yet without the existing vacancies (included for the samples 2, 3 and 5) are taken into the consideration: (1) celestines as monomineral phases, with previously characterized apfu's (Table 1), including the theoretical ionic radiuses of the M cations with occupancies of the twelve-coordination site (Table 2) that are further recalculated (Tables S11 and S12 in the ESM), and (2) as the major celestines with the neglected gypsum or anhydrite phases (including the previously determined apfu's; Table S6 in the ESM). The recalculation includes the theoretical ionic radiuses of the M cations and occupancies of the twelve-coordination site (Table S7 in the ESM), which are presented at Tables S13 and S14 in the ESM. The correlations of the recalculated ionic radiuses (Tables S12 and S14 in the ESM) by the  $a_0$ ,  $b_0$ ,  $c_0$  and  $V_0$  parameters are: (1) 0.884; 0.957; 0.955 and 0.927, respectively [C(12); Figure S20 in the ESM], including (2) 0.126; 0.102; 0.113 and 0.098, respectively [C(13); Figure S21 in the ESM]. Therefore, the first option [C(12)] shows the best fit of all of the available correlations associated with the problem of the ionic radiuses by unit-cell parameters variations [*i.e.* C(3)-C(8)]. On the contrary, the second option [C(13)] shows the lowest correlativity of all of these correlations.

Finally, the newly calculated unit-cell parameters are characterized on the basis of the apfu's (Table S11 in the ESM) and are presented in Table S15 in the ESM. The correlations between these  $a_0$ ,  $b_0$ ,  $c_0$  and  $V_0$  values, with those of the XRPD method (Table 4) having 0.884; 0.955; 0.959 and 0.936, respectively [C(14); Figure S22 in the ESM] have, in this case, a considerably good and significantly better correlation, than the previous one associated with this problematic [*i.e.* C(11); Table S9 and Figure S19 in the ESM]. These observations corroborate that the existing vacancies in the structures of the samples 2, 3 and 5 [C(9) and C(10); Figures S17 and S18 in the ESM] do not have any significant impact on their unit-cell parameters. Such a good correlativity further leads to the final conclusion that entire set of 1-5 samples should be interpreted exclusively as a monomineral celestine near-end members, in the agreement with the SEM-WDS, XRPD and IR results. Therefore, the correlativity allows definitively rejecting the option (iii) as a possible cause for the previously discussed disagreements. In addition, in a such manner, it is possible to provide explanation for the slightly better correlation in the cases of the higher similarity for any purpose of their previous comparison, *i.e.* C(7) vs. C(8) and C(9) vs. C(10) (Figures S15, S16, S17 and S18 in the ESM).

(b) The results in the Tables S9 and S15, show that there is a slightly different ratio between various crystallographic axes, such as  $c_0 < a_0 < b_0$  (samples 1 and 4),  $a_0 < c_0 < b_0$  (samples 2 and 3) and  $a_0 = c_0 < b_0$  (sample 5). Such different ratios indicates the presence of the axial anisotropy, which was previously observed and studied for the synthetic and natural end members of the barite group of minerals (see for examples: Kuang et al. 2017; Li et al. 2018; Girard et al. 2019; Ye et al. 2019; and references therein). This phenomenon appears in the conditions recording an increase of the temperature environment (axial expansion anisotropy) and

elevated formation pressure (axial compression anisotropy) conditions. To the best of our knowledge, there is a lack of similar experiments hitherto dealing with the solid-solutions between minerals within the barite group. Accordingly, we further recalculated the variations of the temperature dependence by the unit-cell parameters for the  $\text{Cl}_{98}\text{Ang}_{02}$ ,  $\text{Cl}_{96}\text{Ang}_{04}$  and  $\text{Cl}_{94}\text{Ang}_{06}$  celestine-anglesite (Table S16 in the ESM), and for the  $\text{Cl}_{99}\text{Brt}_{01}$ ,  $\text{Cl}_{98}\text{Brt}_{02}$  and  $\text{Cl}_{97}\text{Brt}_{03}$  celestine-barite (Table S17 in the ESM) solid-solution series [mineral name symbols such as Ang, Brt and Clt refer to anglesite, barite, and celestine, respectively (Warr, 2021)]. These recalculations use the combination of the initial experimental data at the ambient pressure for anglesite (Li et al. 2018), and celestine and barite (Ye et al. 2019); according to the suitable cell transformation from the  $Pbnm$  (II) to the  $Pnma$  (I) space group, constrained as follows:  $a_{0I}=b_{0II}$ ,  $b_{0I}=c_{0II}$ , and  $c_{0I}=a_{0II}$ . The resulting data (Tables S16 and S17 in the ESM) are further used for the construction of Fig. 4. In addition, we also calculated expansion degree of the unit-cell parameters (*i.e.*, their ratio) of celestine, anglesite and barite between 320K and 520K (Table S18 in the ESM).

By using the recalculated theoretical ionic radiuses of the M cations (Table S12 in the ESM), the excesses of the  $\text{Sr}^{2+}$ ,  $\text{Ca}^{2+}$  and  $\text{Ba}^{2+}$  apfu's, reaching over 1.44 Å, are converted as the total  $\text{Pb}^{2+}$ , *i.e.* as the anglesite 1.40-3.10 mol. % content in celestine. Similarly, the excesses of  $\text{Sr}^{2+}$ ,  $\text{Ca}^{2+}$  and  $\text{Pb}^{2+}$  apfu's over 1.44 Å are converted as the total  $\text{Ba}^{2+}$ , *i.e.* as the barite 0.41-0.91 mol. % content in celestine (Table 7). Subsequently, the Ang and Brt values (Table 7, plotted at Fig. 4) further allowed the estimation of the formation temperatures for the investigated 1-5 celestine samples by using their determined unit-cell parameters (Table 4). The results show that a set of very similar temperatures are characterizing both, the celestine-anglesite and the celestine-barite solid-solution series. In that manner, we have the confirmation that the recalculated Ang and Brt values are valid. The results clearly exhibit that the sample 2 underwent lowest temperatures reaching as low as ~368K, whereas the sample 4 was under the exposure to higher most temperature range reaching ~430K. The samples 1, 3 and 5 were formed at very similar average temperatures of ~387K, ~384K and ~387K, respectively. Therefore, the sampled celestines were formed at the ~368-430K (~95-157 °C) temperature range, at the ambient pressure conditions. Different correlations between the crystallographic axes are  $b_0 < a_0 < c_0$  (samples 1 and 4) and  $a_0 < b_0 < c_0$  (samples 2, 3 and 5).

At last, we provide the explanation of the discussed discrepancies between the WDS and the XRPD results. Namely, Figure S23 in the ESM contains five possible variations (plotted from Fig. 4h; should be taken into account only as an example, because of its validity for each of the other  $a_0$ ,  $b_0$  and  $c_0$  unit-cell axes, including the Ang contents): 1. volume increase by temperature increase, including the Brt contents increase; 2. volume increase by constant temperature, including the Brt contents increase; 3. volume increase by temperature decrease, including the Brt contents increase; 4. constant volume by temperature increase, including the Brt contents decrease; and 5. volume increase by temperature increase, having a constant Brt content. We underline that each of these possible interpretations could be also *vice versa*. In our favorable case, we concluded that the investigated celestine 1-5 samples, are mostly with the first variation type, having partially the fifth variation type, *i.e.*, that their unit-cell parameters increased mainly accounting a temperature increase, whereas the Ang and the Brt contents are reaching almost the constant (*i.e.*, having a small content difference of  $\Delta_{\text{Ang}}=1.70$  mol. %, and  $\Delta_{\text{Brt}}=0.50$  mol. %; Table 7) following the increase status. Because the samples 3 and 5 were exposed to higher temperatures than the sample 2, whereas the sample 4 was formed at a higher

temperature than the sample 1, the former has larger thermal expansions of the unit-cell parameters than the latter. This is the main reason for the average  $2 < 3 < 1 \sim 5 < 4$  and  $2 < 3 \sim 1 = 5 < 4$  variation behaviors (Tables 4 and 7, respectively). In addition, the samples 3 and 5 have larger expansion of the  $b_0$  axis, reaching values over even the sample 1; other possible interpretation is that the sample 1 was formed at a higher pressure by comparing to the samples 3 and 5, because this axis is the most compressible (Kuang et al. 2017; Ye et al. 2019). Accordingly, we strongly believe that this argument is sufficient evidence, supporting the interpretation that the formation temperature is the primary cause, whereas different inserted cations into the structure should be interpreted as a secondary factor for the unit-cell parameters variations of celestine. To underline these observations in a more simplified manner, there is almost a perfect correlativity C(15) of the average temperature dependence (Table 7) by the  $a_0$ ,  $b_0$ ,  $c_0$  and  $V_0$  unit-cell parameters (Table 4) of 0.965; 0.951; 0.991 and 0.997, respectively (Figure S24 in the ESM). The correlation is superior comparing to the C(12) correlation of the celestine composition (Figure S20 in the ESM).

By using the extrapolated data (Tables S16 and S17 in the ESM; Table 7 and Fig. 4) we, moreover, estimate the unit-cell parameters of the studied samples formed at a near-room temperature (23 °C), under the ambient pressure conditions (Table S19 in the ESM). The resulting data are used exclusively for the characterization of the relative unit-cell parameters (Table 8). In this case, a wide range of the correlations between the crystallographic axes are observed:  $b_0 < c_0 < a_0$  (samples 1 and 4),  $a_0 < b_0 < c_0$  (sample 2),  $a_0 < c_0 < b_0$  (sample 3), and  $c_0 < b_0 < a_0$  (sample 5).

The results have almost a perfect correlation C(16) of the average temperature dependence (Table 7), by the  $a_0$ ,  $b_0$ ,  $c_0$  and  $V_0$  ratios (Table 8) of 0.979; 0.926; 0.988 and 0.998, respectively (Figure S25 in the ESM). These are, as expected, very similar to the C(15) correlations, relative to the temperature by the unit-cell parameters variations (Figure S24 in the ESM). In addition, the linear and the polynomial variations have almost the same values in these two cases.

The synthesis of data (Tables 7 and 8; Figure S25 in the ESM), allowed us to additionally construct the variation diagram of the relative  $a_0$ ,  $b_0$ ,  $c_0$  and  $V_0$  unit-cell parameters (*i.e.*, their ratios) by the temperature dependence of the studied samples at the ambient pressure conditions (Fig. 5). Importantly, the resulting variation diagram has the fits (*i.e.* for all of the five samples together) adequate to the celestine  $c_0 < b_0 < a_0$  crystal growth expansive behavior (see Figs. 11b and 12b at Ye et al. 2019; and Table S18 in the ESM). Taking into account solemnly the crystal expansion caused by temperature (Table 7), the samples 1 and 4 are showing the variations that are similar to that of barite, whereas the samples 2, 3 and 5 show the variations similar to that of celestine (Ye et al. 2019; and Table S18 in the ESM). By interpreting the structural aspect (Antao 2012), the first group of samples are less distorted, in comparison with the second, being in the agreement with the geometry change of the  $SO_4$  and  $MO_{12}$  polyhedral, which were influenced mainly by the vacancies present for the latter ones (already discussed before). On the other hand, taking into account solemnly the crystal compression by pressure (Table 8), it appears that the sample 4 was also formed at a considerably higher pressure (similarly to sample 1) relative to the samples 2, 3 and 5 because of their identical axes variations.

## 5.2. Consideration about the celestine minerogenesis and other possible formation conditions

In this part, we take into the consideration other celestine formation conditions, in particular, typifying shallow crustal and marine environments (Hanor 2000). The results indicate that the celestines were formed at ~368-430K (~95-157 °C) temperature range, at the ambient pressure conditions (Table 7). Consequently, we take into the consideration the following options for the celestine minerogenesis: 1. temperature remains constant by a pressure increase; 2. temperature increase by a pressure increase; and 3. temperature increase by a pressure decrease (Figure S26a in the ESM). Following the experimental data (Kuang et al. 2017; Li et al. 2018; Girard et al. 2019; Ye et al. 2019), we believe that if the subsurface pressure increases, temperatures should also follow a pressure increase. The latter phenomenon occurs accounting the axial compression, which should be simultaneously compensated by the axial expansion, so that the unit-cell parameters remain unchanged (*i.e.* as already previously characterized; Table 4). Accordingly, we have chosen the second option, because the other two options led exclusively to the smaller unit-cell parameters. This scenario is graphically outlined by the yellow full lines at Figure S26a in the ESM. The increasing slope is approximated, accounting the lacking of the appropriate experimental data for the formation pressure. The increase of the formation pressure allowed us to put constraints, evaluating the probable subsurface conditions under which the investigated crystals could have been formed. For example, if we presume that the pressure was 250 bars, accordingly, the temperature range becomes a slightly higher, *ca.* 372-434K (~99-161 °C) fitting into the volcanic areas.

On the other hand, subsidence and deposition within sedimentary basins yields higher pressures than that observed within the investigated volcanic areas. By presuming a pressure increase, reaching up to 500, 750, 1000 and 1250 bars, the temperature range may increase reaching ~382-444K (~109-171 °C), ~391-453K (~118-180 °C), ~429-482K (~147-209 °C), and ~452-514K (~179-241 °C), respectively (Figure S26a in the ESM). By combining the data, we additionally constructed a wider range, allowing further narrowing of the celestine formation area/depth. As a result, the celestine minerogenesis could originate from the following subsurface conditions:

1. from ~382K (~109 °C; sample 2), over ~417K (~144 °C; sample 1), to ~482K (~209 °C; sample 4), at 500, 750 and 1000 bars, respectively (Figure S26b in the ESM); or
2. from ~372K (~99 °C; sample 2), over ~412K (~139 °C; sample 1), to ~453K (~180 °C; sample 4), at 250, 500 and 750 bars, respectively (Figure S26c in the ESM).

We underline that these values have rather a speculative character, because constrained on reasonable temperature and pressure ranges reaching 373-473K (~100-200 °C), formed at a range from 250 to 1000 bars.

Contributing further to the higher-pressure conditions, result fits additionally into a different compression behavior of the unit-cell axes. According to Kuang et al. (2017), the study proposes that the  $b_0$  axis is the most compressible, whereas the  $a_0$  axis is the most incompressible for celestine. The authors explained this in the following manner: "*Although the  $b_0$  axis is the shortest crystallographic axis in celestine, the largest bond distance of Sr-O is also parallel to the  $b_0$  axis in celestine structure. Therefore, the bonding force between Sr-O*

*in this direction is the weakest and thus results in the  $b_0$  axis being the most compressible axis".* Such behavior is clearly visible in the samples 1 and 4 (already mentioned earlier in the text, Table 8), explaining a lowermost  $b_0$  by  $a_0$  correlativity among the unit-cell parameters (Figures S7d and S8a in the ESM).

There are additional facts contributing the final conclusions are as follows:

1. The celestines collected from the Al Gata member (formation Wadi Thámat) occurring as a larger accumulation in the clayey, slightly carbonate sedimentary rocks;
2. These sedimentary formations carrying the investigated celestine are top-sealed by the younger basalt outflows;
3. The celestines are originated from druses or clusters exposed at the surface outcrop scale;
4. In addition, rare occurrences of fibrous celestine are observed too, representing the resulting pseudomorphosis of fibrous gypsum;
5. Other minerals identified in a close vicinity of celestine are quartz, gypsum, anhydrite, calcite and aragonite (Rundić and Daloub 2007; Vasić and Sheriff 2007; Rundić et al. 2012);
6. The investigated celestine is a mineral that usually precipitates when Sr-bearing fluids, reach contact with sulphate-rich solutions (or rocks in various sedimentary settings), probably developed over a large temperature range (25–200 °C; Hanor 2000, 2004); and
7. Forjanec et al. (2020) reported that the gypsum-to-celestite transformation rapidly advances, once interacting with a Sr-bearing solution. During the process of interacting with a Ba-bearing solution, gypsum barely transforms into barite, regardless of the length of the interaction.

Finally, we conclude that the Jabal Eghei celestines were formed as the secondary minerals in the position over a gypsum and/or anhydrite layer (as a source of S and Ca). The celestine formation have occurred after the interaction with a hydrothermal (Sr, Pb and Ba)-bearing solution, most probably sourced from the basalt extrusion-related activity (Radivojević et al. 2015). These elements (Ba, Sr, Pb) are dominantly sourced by the 1<sup>st</sup> and 2<sup>nd</sup> volcanic extrusion stage, in particular the Pb (Radivojević et al. 2015). The temperatures are over ~368K (~95 °C), and at pressures over 250 bars. Considering that the first basalt extrusion phase occurred during the Middle to Late Miocene time (basalts show a K/Ar age range from  $16.1 \pm 2.9$  Ma to  $7.9 \pm 2.3$  Ma), and the second phase is of Late Miocene to Pliocene age ( $7.19 \pm 0.36$  Ma and  $4.32 \pm 0.35$  Ma; Radivojević et al. 2015), the emplacement of the celestine-bearing brine could have occurred prior the phase 3 or the 3<sup>rd</sup> volcanic extrusion stage. By comparing the hypothetical pressure condition (Figure S26b,c in the ESM, green color), we argue that the tentative age of the celestine formation, is after the deposition and exposure to the successor erosional stage of the Wadi Thámat formation. Considering that the age of the weather crust (location of the celestine druses) is after the 1<sup>st</sup> volcanic stage, the age should be similar to the oldest basalts.

## 6. Conclusion

Five celestine crystals are analyzed and characterized for the minerogenesis by applying the SEM-WDS, XRPD and IR methods. Their chemical composition is mutually very similar, and fits into the monomineral celestine near-end members in which only 1.6-4.1 at. % of  $\text{Sr}^{2+}$  contents were substituted by  $\text{Pb}^{2+}$ ,  $\text{Ba}^{2+}$ ,  $\text{Ca}^{2+}$  and the

vacancies (in three samples). We further provide the constraints on the minerogenesis, emphasizing that the resulting subsurface temperatures represent the primary cause for the celestine formation. The constraints on the differently inserted cations into the structure are characterized as a secondary factor for the unit-cell parameters, including the observed slight  $c_0 < b_0 < a_0$  axial anisotropy variations. The investigated celestines were likely formed as a secondary, positioned over gypsum and/or anhydrite, at the temperatures over  $\sim 373\text{K}$  ( $\sim 100\text{ }^\circ\text{C}$ ) and pressures over 250 bars. Three celestine samples have greenish-blue to blue color, whereas the other two samples are of blue-green (cyan) color. In addition, the celestine minerogenesis study of the Jabal Eghei area corroborated that the coefficients of the regression- $R^2$  may represent a very useful accessory tool that is applicable for the minerals comparison purposes, or once correlating a variety of available parameters.

Unfortunately, the correlations between the color purities of the investigated celestines according to their chemical compositions, unit-cell dimensions, formation conditions, or any other investigated parameter have not been highlighted in this study. With exception of the larger vacancy content in the sample 5, the most prominent difference of the color purity ranges between the samples 3 and 5. These samples have very similar results, yielded by a number of methods used throughout this study. In summary, further experiments are necessary for resolving this problem.

## Declarations

**Declaration of competing interest:** The authors have no competing interests to declare.

Ethics approval and consent to participate

Authors guarantee that the study in original not submitted in any other journal

Consent for publication

If the manuscript is accepted for publishing, authors give consent for publishing

Author contributions

P.T. and D.S. wrote the main manuscript text. P.T., M.M., B.K., A.K. and M.P.-S. performed the experiments and analyzed data. P.T., D.S. and J.K. prepared figures 1-5. P.T., D.S., M.M., B.K. and A.K. prepared supplementary material. All authors reviewed the manuscript.

Funding

This research did not receive any specific grant from funding agencies in the public, commercial or not-for-profit sectors.

Availability of data and materials

Data are available in Supplementary electronic material.

## References

1. Abadi AM, Van Wees J, Van Dijk MP, Cloetingh SA (2008) Tectonic and subsidence evolution of the Sirt Basin, Libya. *AAPG Bulletin* 92:993–1027 <https://doi.org/10.1306/03310806070>
2. Abdusahmin FA (2020) Geology and potentiality of basalts in Jabal Eghei area (Libya). Dissertation, Faculty of Mining and Geology, Belgrade, Serbia
3. Antao SM (2012) Structural trends for celestite (SrSO<sub>4</sub>), anglesite (PbSO<sub>4</sub>), and barite (BaSO<sub>4</sub>): Confirmation of expected variations within the SO<sub>4</sub> groups. *Am Mineral* 97:661-665 <http://dx.doi.org/10.2138/am.2012.3905>
4. Ashour A, Jonathan P, Phillipe D et al (2012) New insight into the sedimentology and stratigraphy of the Dur At Talah tidal-fluvial transition sequence (Eocene–Oligocene, Sirt Basin, Libya). *J Afr Earth Sci* 65:72–90 <https://doi.org/10.1016/j.jafrearsci.2012.02.004>
5. Berar JF, Lelann P (1991) E.S.D.'s and estimated probable error obtained in Rietveld refinements with local correlations. *J Appl Cryst* 24:1–5 <https://doi.org/10.1107/S0021889890008391>
6. Bernstein LR (1979) Coloring mechanisms in celestite. *Am Mineral* 64:160-168
7. Bershov LV, Marfunin AS (1967) Paramagnetic resonance of electron-hole centers in minerals. *Dokl Akad Nauk SSSR*, 173:410-412
8. Bishop JL, Murad E (2005) The visible and infrared spectral properties of jarosite and alunite. *Am Mineral* 90:1100-1107 DOI: 10.2138/am.2005.1700
9. Brigatti MF, Galli E, Medici L (1997) Ba-rich celestine: new data and crystal structure refinement. *Mineral Mag* 61:447–451
10. Capitanio FA, Faccenna C, Funiciello R, (2009) The opening of Sirte basin: results of slab avalanching?. *Earth Planet Sci Lett* 285:210–216 <https://doi.org/10.1016/j.epsl.2009.06.019>
11. Commission Internationale de l'Eclairage (1932) 1931 Commission Internationale de l'Eclairage Proceedings. Huitième session. pp. 19–29. Cambridge, UK, Cambridge University Press.
12. Clark RN (1999) Chapter 1: Spectroscopy of Rocks and Minerals, and Principles of Spectroscopy. In A.N. Rencz, Ed., *Manual of Remote Sensing, Remote Sensing for the Earth Sciences*, 3:3-58. John Wiley and Sons, New York.
13. Cvetković, V, Toljić M, Ammar NA, Rundić Lj, Trish KB (2010) Petrogenesis of the eastern part of the Al Haruj basalts (Libya). *J Afr Earth Sci* 58:37–50 <https://doi.org/10.1016/j.jafrearsci.2010.01.006>
14. Cvetković Ž, Tančić P (2019) Mineralogical and crystallographic characteristics of bauxites from some Grebnik's (Metohija, Serbia) ore deposits, *Geol an Balk poluos* 80(1):45–61 <https://doi.org/10.2298/GABP19010045C>
15. Deer W, Howie R, Zussman J (2013) Celestine. In: *An Introduction to the Rock-Forming Minerals*, 3rd edn The Mineral Society: London, UK, pp. 444
16. Doelter C (1915) *Die Farben der Mineralien*. Fried. Vieweg und Sohn, Braunschweig, Germany
17. Elshaafi A, Gudmundsson A (2016) Volcano-tectonics of the Al Haruj Volcanic Province, Central Libya. *J Volcanol Geotherm Res* 325:189–202 [10.1016/j.jvolgeores.2016.06.025](https://doi.org/10.1016/j.jvolgeores.2016.06.025)
18. Forjanés P, Astilleros JM, Fernández-Díaz L (2020) The Formation of Barite and Celestite through the Replacement of Gypsum. *Minerals*, 10(2):189 <https://doi.org/10.3390/min10020189>

19. Friend JN, Allchin JP (1939) Colour of celestine. *Nature*, 144, 633
20. Friend JN, Allchin JP (1940) Colloidal gold as a colouring principle in minerals. *Mineral Mag* 25:584-596
21. Gadsden JA (1975) *Infrared Spectra of Minerals and Related Inorganic Compounds*. Butterworth & Co. (Publishers) Ltd., London
22. Garske D, Peacor DR (1965) Refinement of the structure of celestite  $\text{SrSO}_4$ . *Z Kristallogr* 121:204–210
23. Girard A, Stekiel M, Spahr D et al (2019) Structural, elastic and vibrational properties of celestite,  $\text{SrSO}_4$ , from synchrotron x-ray diffraction, thermal diffuse scattering and Raman scattering. *J Phys Condens Matter* 31:055703 <https://doi.org/10.1088/1361-648X/aaf0ef>
24. Goldish E (1989) X-ray diffraction analysis of barium strontium sulfate (barite-celestite) solid solutions. *Powder Diffr* 4:214-216 <https://doi.org/10.1017/S0885715600013750>
25. Guirguis LA (1987) Infrared vibrational sulphate band shift correlation in alkaline sulphate minerals. *TIZ-Fachberichte* 111: 339-340
26. Hallett D (2002) *Petroleum Geology of Libya*. Elsevier, Amsterdam, 503p.
27. Hanor JS (2000) Barite-Celestine Geochemistry and Environments of Formation. In: Alpers CN, Jambor JL, Nordstrom DK (eds) *Sulfate Minerals-Crystallography, Geochemistry, and Environmental Significance Reviews in Mineralogy and Geochemistry* 40. Virginia: Mineralogical Society of America, Chantilly, pp 193–275
28. Hanor JS (2004) A model for the origin of large carbonate- and evaporite-hosted celestine ( $\text{SrSO}_4$ ) deposits. *J Sediment Res* 74:168–75 <https://doi.org/10.1306/092203740168>
29. Hawthorne FC, Ferguson RB (1975) Anhydrous sulphates. I. Refinement of the crystal structure of celestite with an appendix on the structure of thenardite. *Can Mineral* 13:181–187
30. Hezel A, Ross SD (1966) Forbidden transitions in the infra-red spectra of tetrahedral anions - III. Spectra-structure correlations in perchlorates, sulphates and phosphates of the formula  $\text{MXO}_4$ . *Spectrochim Acta*, 22, 1949-1961 [https://doi.org/10.1016/0371-1951\(66\)80183-2](https://doi.org/10.1016/0371-1951(66)80183-2)
31. Herzberg G (1945) *Infrared and Raman Spectra of Polyatomic Molecules*. Van Nostrand, New York
32. ICDD-PDF 05-0593 (1953) Celestine, Swanson, Fuyat, National Bureau of Standards (U.S.), Circ. 539, II, 61
33. ICDD-PDF 24-1035 (1972) Barite, National Bureau of Standards (U. S.) Monograph, 25, 10, 12
34. ICDD-PDF 36-1461 (1986) Anglesite, McMurdie et al., *Powder Diffr* 1, 70
35. ICDD-PDF 37-1496 (1986) Anhydrite, McMurdie et al., *Powder Diffr* 1, 267
36. ICDD-PDF 89-0953 (1998) Strontium Sulfate, Burger K, Cox D, Papoular R, Prandl W, *J Appl Cryst* 31:789
37. Isetti G (1970) Studio sulla colorazione della celestina. *Doriana*, 4, no. 194, 1-7
38. Jacobsen SD, Smyth JR, Swope RJ, Downs RT (1998) Rigid-body character of the  $\text{SO}_4$  groups in celestine, anglesite and barite. *Can Mineral* 36:1053–1060
39. Kloprogge JT, Ruan H, Duong LV, Frost RL (2001) FT-IR and Raman microscopic study at 293 K and 77 K of celestine,  $\text{SrSO}_4$ , from the middle triassic limestone (Muschelkalk) in Winterswijk, The Netherlands. *Geologie en Mijnbouw/Netherlands Journal of Geosciences* 80(2): 41-47 <https://doi.org/10.1017/S0016774600022307>

40. Kuang Y, Xu J, Zhao D et al (2017) The high-pressure elastic properties of celestine and the high-pressure behavior of barite-type sulphates. *High Temp High Press* 46:481–495
41. Lane MD (2007) Mid-infrared emission spectroscopy of sulfate and sulfate-bearing minerals. *Am Mineral* 92:1-18 DOI: 10.2138/am.2007.2170
42. Le Bail A, Duroy H, Fourquet JL (1988) Ab-initio structure determination of  $\text{LiSbWO}_6$  by X-ray powder diffraction, *Mater Res Bull* 23(3):447-452 [https://doi.org/10.1016/0025-5408\(88\)90019-0](https://doi.org/10.1016/0025-5408(88)90019-0)
43. Li B, Xu J, Chen W et al (2018) Compressibility and expansivity of anglesite ( $\text{PbSO}_4$ ) using in situ synchrotron X-ray diffraction at high-pressure and high-temperature conditions. *Phys Chem Miner* 45:883–893 <https://doi.org/10.1007/s00269-018-0970-1>
44. Miyake M, Minato I, Morikawa H, Iwai S (1978) Crystal structures and sulphate force constants of barite, celestite, and anglesite. *Am Mineral* 63:506–510
45. Moenke H (1959) *Mineralspektren I: Die Ultrarotabsorption der häufigsten und wirtschaftlich wichtigsten Halogenid-, Oxyd-, Hydroxyd-, Carbonat-, Nitrat-, Borat-, Sulfat-, Chromat-, Wolframat-, Molybdat-, Phosphat-, Arsenat-, Vanadat- und Silikatminerale im Spektralbereich 400-4000  $\text{cm}^{-1}$* . Akademie Verlag, Berlin.
46. Nakamoto K (1986) *Infrared and Raman Spectra of Inorganic and Coordination Compounds*. Wiley and Sons, New York
47. Omori K (1986) Infrared diffraction and the far infrared spectra of anhydrous sulfates. *Mineralogical Journal* 5:334-354 <https://doi.org/10.2465/minerj1953.5.334>
48. Palache C, Berman H, Frondel C (1951) *Dana's system of mineralogy*, 7th ed., v. II, John Wiley & sons, London, UK, pp. 415–420.
49. Radivojević M, Toljić M, Turki S et al (2015) Neogene to Quaternary basalts of the Jabal Eghei (Nuqay) area (south Libya): Two distinct volcanic events or continuous volcanism with gradual shift in magma composition? *J Volcanol Geotherm Res* 293:57–74 <http://dx.doi.org/10.1016/j.jvolgeores.2015.02.003>
50. Ross SD (1972) *Inorganic Infrared and Raman Spectra*. McGraw-Hill Book Company (UK) Ltd., London
51. Ross SD (1974) Sulphates and other oxy-anions of group VI. In: *The Infrared Spectra of Minerals*, V.C. Farmer (ed), *Mineralogical Society Monograph* 4:423-444 <https://doi.org/10.1180/mono-4.18>
52. Rundić Lj, Dalub H (2007) Geological map of Libya 1:250 000. Sheet Dur Al Abrag (NG 34–5). Explanatory Booklet. Industrial Research Center, Tripoli. 110 pp.
53. Rundić Lj, Toljić M, Vasić N et al (2012) Tertiary Formations of the SW Part of Sirt Basin: New Stratigraphic and Sedimentological Data. *Geology of Southern Libya* 1:153-174
54. Rusk DC (2001) Libya: Petroleum potential of the underexplored basin centers—A twenty-first-century challenge, in MW Downey, JC Threet, and WA Morgan (eds), *Petroleum provinces of the twenty-first century: AAPG Memoir* 74, p. 429–452
55. Schulman JH, Compton WD (1962) *Color Centers in Solids*. Macmillan, New York
56. Serna CJ, Cortina CP, Ramos JVG (1986) Infrared and Raman study of alunite-jarosite compounds. *Spectrochim Acta* 42A:729-834 DOI: 10.1016/0584-8539(86)80092-7
57. Shannon RD (1976) Revised Effective Ionic Radii and Systematic Studies of Interatomic Distances in Halides and Chalcogenides, *Acta Crystallogr* A32:751-767 <https://doi.org/10.1107/S0567739476001551>

58. Stromeyer F (1821) Untersuchungen über Mischung der Mineralkörper, vol. 1. Vandenhoeck und Ruprecht, Göttingen
59. Takahashi S, Seki M, Setoyama K (1993) Formation of  $\text{SrSO}_4 \cdot 1/2\text{H}_2\text{O}$  in an  $\text{SrSO}_4\text{--H}_2\text{O}$  System and Its Solid Solution in a  $\text{CaSO}_4\text{--SrSO}_4\text{--H}_2\text{O}$  System, *Bulletin of the Chemical Society of Japan* 66(8):2219-2224 <https://www.journal.csj.jp/doi/10.1246/bcsj.66.2219>
60. Tančić P (2017) Comparison of the crystallographic-chemical characteristics of sphalerites from the Kiževak ore deposit with some other deposits, part I: Preliminary reconsideration about their formation conditions. *Bulletin of Mines CXIV (1-2)*:101–117 Doi: 10.25075/BM.2017.11
61. Tančić P (2018) Comparison of the crystallographic-chemical characteristics of sphalerites from the Kiževak ore deposit with some other deposits, part II: Construction of the four-component  $a_0\text{-FeS-P-T}$  diagram (option I) and determination of the formation conditions. *Bulletin of Mines CXV (1-2)*:59–73 Doi: 10.25075/BM.2018.04
62. Tančić P, Kremenović A (2022) Rietveld crystal structure refinement of the natural rhombohedral grossular-andradite garnet from Serbia, *Geol Q* 66(7):1639 doi: 10.7306/gq.1639
63. Tančić P, Kremenović A, Vulić P (2020) Structural dissymmetrization of optically anisotropic  $\text{GrS}_{64\pm 1}\text{Adr}_{36\pm 1}\text{Sps}_2$  grandite from Meka Presedla (Kopaonik Mt., Serbia), *Powder Diffr* 35(1):7-16 <https://doi.org/10.1017/S0885715619000897>
64. Tančić P, Dimitrijević R, Poznanović M, Pačevski A, Sudar S (2012) Crystal structure and chemical composition of ludwigite from Vranovac ore deposit (Boranja Mountain, Serbia), *Acta Geol Sin-Engl* 86(6):1524-1538 DOI: 10.1111/1755-6724.12020
65. Tančić P, Spahić D, Jovanović D, Ćirić A, Poznanović-Spahić M, Vasić N (2021) Occurrences and characterization of alunite group minerals from the Lece-Radan Oligo-Miocene volcanic complex (Serbia), *Geol Q* 65(19):1587 doi: 10.7306/gq.1587
66. Toljić M, Agrab AFM (2014) Geological map of Libya 1:250 000. Sheet Wādi Eghei (NF 34-1). Explanatory Booklet. Industrial Research Center, p. 305. Tripoli (in print)
67. Toljić M, Agrab AFM (2016) Explanatory Booklet, Sheet: Wadi Eghei (NF 34-1). Geological map of Libya 1:250,000, Industrial Research Centre, Libya, Tripoli. p. 30. (in print)
68. Toljić M, Marović M, Kovačević J et al (2007) Explanatory booklet for the Geological map of Libya, 1:250 000 Sheet NF 34-1. 326 pp., Beograd – Tripoli.
69. Vasić N, Sherif KA (2007) Geological map of Libya 1: 250,000. Sheet: Dur-At-Talah (NG 34-9). Explanatory Booklet. Industrial Research Centre, Libya. Tripoli. 180pp.
70. Vassallo AM, Finnie KS (1992) Infrared emission spectroscopy of some sulfate minerals. *Appl Spectrosc* 46:1477-1482 <https://doi.org/10.1366/000370292789619296>
71. Warr LN (2021) IMA–CNMNC approved mineral symbols. *Mineral Mag* 85:291–320 <https://doi.org/10.1180/mgm.2021.43>
72. Wittstein GC (1856) Ueber die Ursache der blauen Farbe des Coelestins. *Vierteljahresschrift für Praktische Pharmacie*, 5:286-287
73. Ye Z, Li B, Chen W et al (2019) Phase transition and thermoelastic behavior of barite-group minerals at high-pressure and high-temperature conditions. *Phys Chem Miner* 46:607–621

## Tables

**Table 1** The resulting WDS analyses of the 1-5 studied samples (in wt. %). Atoms per formula units (hereinafter apfu; in at. %) are calculated at the 4 oxygen anions basis

oxides	Sample 1	Sample 2	Sample 3	Sample 4	Sample 5
<b>SrO</b>	55.21	54.72	54.93	54.93	54.33
<b>CaO</b>	0.07	0.16	0.15	0.24	0.22
<b>BaO</b>	0.45	0.62	0.42	0.56	0.58
<b>PbO</b>	1.04	0.94	0.87	1.01	0.94
<b>SO<sub>3</sub></b>	43.23	43.57	43.62	43.28	43.93
<b>Σ</b>	100.00	100.00	99.99	100.02	100.00
apfu	Sample 1	Sample 2	Sample 3	Sample 4	Sample 5
<b>Sr</b>	0.984	0.970	0.973	0.978	0.959
<b>Ca</b>	0.002	0.005	0.005	0.008	0.007
<b>Ba</b>	0.005	0.007	0.005	0.007	0.007
<b>Pb</b>	0.009	0.008	0.007	0.008	0.008
<b>ΣM</b>	1.000	0.990	0.990	1.001	0.981
<b>S</b>	1.000	1.003	1.003	1.000	1.006
<b>ΣM+S</b>	2.000	1.993	1.993	2.001	1.987
<b>S/ΣM</b>	1.000	1.013	1.013	0.999	1.025
<b>Σ(Pb+Ba)/Σ(Ca+X)</b>	7.000	1.000	0.800	1.875	0.577

**Table 2** Calculated theoretical ionic radiuses (in Å) of the M cations, and calculated occupancies of the twelve-coordination site (in at. %) at the basis of the determined apfu's (Table 1)

	Sample 1	Sample 2	Sample 3	Sample 4	Sample 5	variations
<b>Sr<sup>2+</sup></b>	1.41696	1.39680	1.40112	1.40832	1.38096	5<2<3<4<1
<b>Ca<sup>2+</sup></b>	0.00268	0.00670	0.00670	0.01072	0.00938	1<2=3<5<4
<b>Ba<sup>2+</sup></b>	0.00805	0.01127	0.00805	0.01127	0.01127	1=3<2=4=5
<b>Pb<sup>2+</sup></b>	0.01341	0.01192	0.01043	0.01192	0.01192	3<2=4=5<1
<b>Σr<sub>M</sub></b>	1.44110	1.42669	1.42630	1.44223	1.41353	5<3<2<1<4
<b>occ.*</b>	1.00076	0.99076	0.99049	1.00155	0.98162	5<3<2<1<4

\*-occupancies were calculated by the Σr<sub>M</sub>/1.44Å ratios

**Table 3** Calculated SrSO<sub>4</sub> mole fractions from the observed  $d_{(211)}$  inter-planar spacings (Table S1 in the ESM)

	Sample 1	Sample 2	Sample 3	Sample 4	Sample 5
<b>observed <math>d_{211}</math> (Å)</b>	2.9708	2.9698	2.9704	2.9737	2.9708
<b>SrSO<sub>4</sub> (mol. %)*</b>	99.8	100.6	100.2	97.6	99.8

\*calculated from the equation by Goldish (1989):  $d(211) = 3.1023 - 0.1317 \times S$ , where S is the SrSO<sub>4</sub> mole fraction

**Table 4** Calculated unit-cell parameters of the investigated samples in the *Pnma* space group, compared to the celestine reference data standards; and also between each other

	89-0953	05-0593	Sample 1	Sample 2	Sample 3	Sample 4	Sample 5	variations
<b>a<sub>0</sub> (Å)</b>	8.359	8.359	8.3622(6)*	8.3578(9)	8.359(1)	8.3705(6)	8.361(1)	2<3<5<1<4
<b>b<sub>0</sub> (Å)</b>	5.350	5.352	5.3519(4)	5.3510(5)	5.353(1)	5.3568(4)	5.3528(8)	2<1<3~5<4
<b>c<sub>0</sub> (Å)</b>	6.869	6.866	6.8702(4)	6.8683(7)	6.8690(8)	6.8767(2)	6.8696(6)	2<3<5<1<4
<b>V<sub>0</sub> (Å<sup>3</sup>)</b>	307.27	307.17	307.46(4)	307.17(5)	307.36(8)	308.34(4)	307.47(7)	2<3<1~5<4

\*-The numbers in parentheses in this and further Tables are the estimated standard deviations (hereinafter esd's) multiplied with Scor (Berar and Lelann, 1991; Table S2 in the ESM), and refer to the last significant number

**Table 5** The summarized IR results for the investigated samples together with the literature data

Sample					Reference						
1	2	3	4	5	1*, 1a*	2*	3*	4*	5*	6*	7*
448	449	448	435	440							
475	475	478	468	470	491						471
		608	602	605			610	610-613	613-		
614	613	612	609	610	613				614	611	614
622	622	632	632		627	620			620		
651	642	645	641	642	642		639	641-644		643	648
655	650					650					
1001	1000	998	995	999	974	1015	990	993-998	993	991	991
1105							1110				
	1089		1085		1081			1086-1096			
	1100	1095		1090			1095			1091	
	1102	1115	1121								
		1130	1128	1138			1130	1131-1145	1133	1138	1138
1152	1151	1155	1150	1158	1147	1150			1150		
				1189	1179						
1198	1194	1195	1192			1200	1195	1190-1207	1197	1201	
1210	1212	1205	1205								
			1222								
1242	1238	1248	1240	1245				1240-1250	1242	1248	1238

References: 1\* Ross (1972); 1a\* Ross (1974); 2\* Guirguis (1987); 3\* Omori (1986); 4\* Gadsden (1975), 5\* Moenke (1956); 6\* Kloprogge et al. (2001); and 7\* Lane (2007).

**Table 6** Dominant wavelength (in nm) and the color purity of the investigated samples. The contents of the organic matter (in wt. %) are also presented

	Sample 1	Sample 2	Sample 3	Sample 4	Sample 5
<b>Dominant wavelength</b>	481.7	482.5	494.1	480.4	489.1
<b>Purity of the color</b>	5.37	4.64	1.36	5.45	7.16
<b>Organic matter</b>	<0.05	<0.05	<0.05	0.14	<0.05

**Table 7** The estimated formation (in K) of the studied samples based on their recalculated anglesite (Ang) and barite (Brt) contents (Fig. 4)

	Sample 1		Sample 2		Sample 3		Sample 4		Sample 5		variations
	Ang	Brt									
<b>mol.%</b>	2.20	0.65	2.18	0.64	1.40	0.41	3.10	0.91	1.78	0.52	3<5<1~2<4
<b>a<sub>0</sub> (Å)</b>	392	385	360	356	370	368	428	427	386	378	2<3<5<1<4
<b>b<sub>0</sub> (Å)</b>	373	378	361	370	386	387	414	418	387	385	2<1<3~5<4
<b>c<sub>0</sub> (Å)</b>	394	407	380	384	393	397	445	451	396	395	2<3~5<1<4
<b>average (axes)</b>	387	390	367	370	383	384	429	432	389	386	2<3<1~5<4
<b>V<sub>0</sub> (Å<sup>3</sup>)</b>	382	383	365	365	382	383	429	430	387	387	2<1~3<5<4
<b>average (all)</b>	386	388	366	369	383	384	429	432	388	386	2<3~1=5<4
<b>average (Ang+Brt)</b>	387		368		384		430		387		2<3~1=5<4
<b>axes variations</b>	b <sub>0</sub> <a <sub>0</sub> <c <sub>0</sub>		a <sub>0</sub> <b <sub>0</sub> <c <sub>0</sub>		a <sub>0</sub> <b <sub>0</sub> <c <sub>0</sub>		b <sub>0</sub> <a <sub>0</sub> <c <sub>0</sub>		a <sub>0</sub> <b <sub>0</sub> <c <sub>0</sub>		

**Table 8** Relative unit-cell parameters of the investigated samples, calculated from the ratio of the data outlined in Table 4 and Table S19 in the ESM (marked here with \*)

	Sample 1	Sample 2	Sample 3	Sample 4	Sample 5	sample variations
$a_0/a^*$	1.00170	1.00117	1.00144	1.00246	1.00156	2<3<5<1<4
$b_0/b^*$	1.00129	1.00112	1.00150	1.00202	1.00146	2<1<3~5<4
$c_0/c^*$	1.00149	1.00121	1.00146	1.00214	1.00140	2<5<3~1<4
average (axes)	1.00149	1.00117	1.00147	1.00221	1.00147	2<1~3~5<4
$V_0/V^*$	1.00444	1.00350	1.00444	1.00667	1.00448	2<1~3~5<4
average (all)	1.00223	1.00175	1.00221	1.00332	1.00222	2<1~3~5<4
ratio of axes variations	$b_0 < c_0 < a_0$	$a_0 < b_0 < c_0$	$a_0 < c_0 < b_0$	$b_0 < c_0 < a_0$	$c_0 < b_0 < a_0$	

## Figures

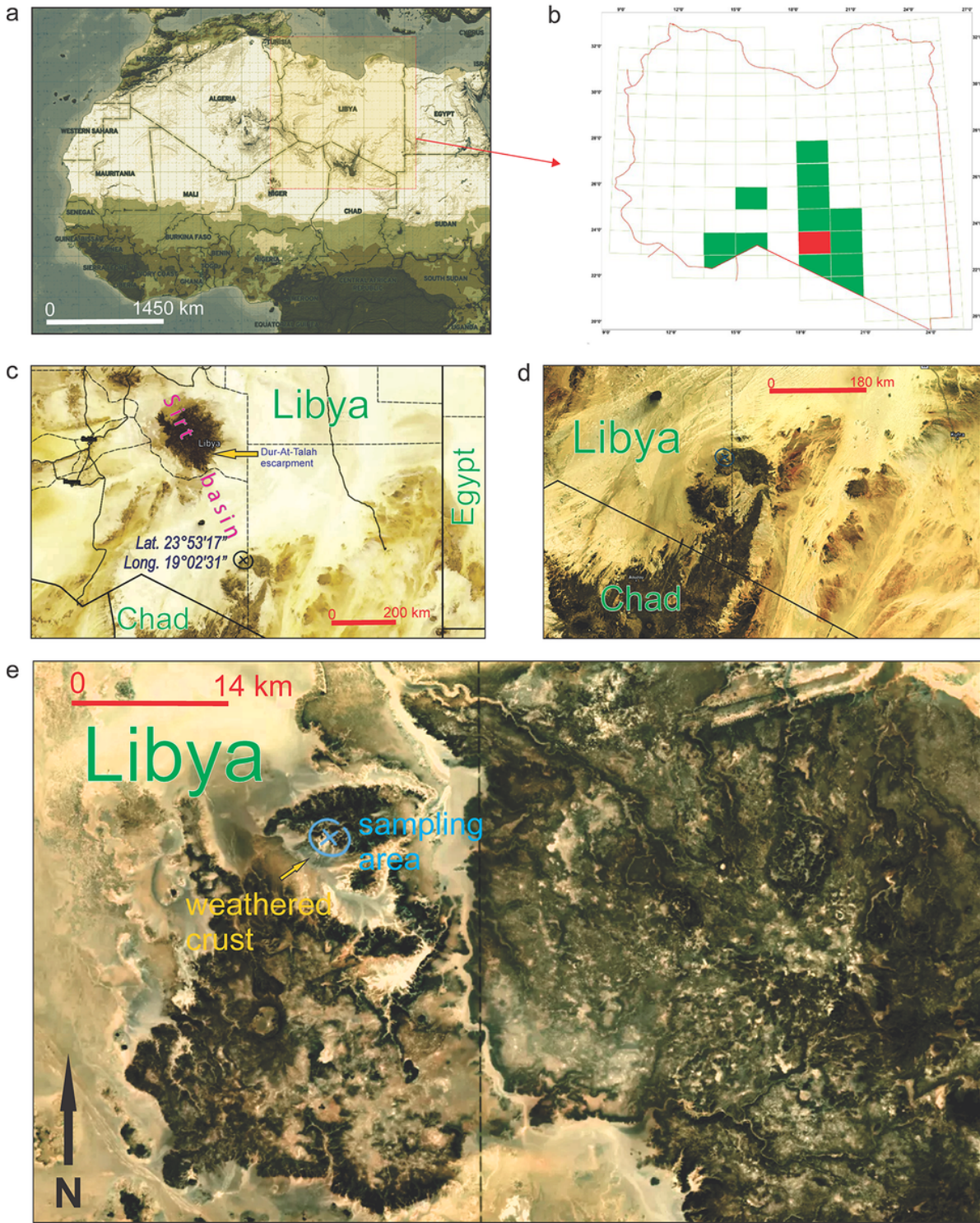


**Figure 1**

**a** The investigated area within the circum-Mediterranean realm; **b** Geological Mapping campaign of central and southern Libya (marked with green color); **c** The wider area of the Al Haruj and Jabal Eghei Volcanic Provinces; **d** Jabal Eghei Volcanic Province; and **e** The surface-exposed basalts as the result of the three Middle Miocene to Pliocene volcanic events (according to Radivojević et al. 2015). The spots of the celestine sampling locations are marked with the “x” symbol, collected from the area of the sheet NF 34-1, Geological Map of Libya, scale 1:250,000 (marked with red color)



**Figure 2**

Occurrences of celestine crystals at the Al Gata member, formation Wadi Thámat (Coordinates: Lat. 23° 53' 17"; Long. 19° 02' 31"). Photo by J. Kovačević

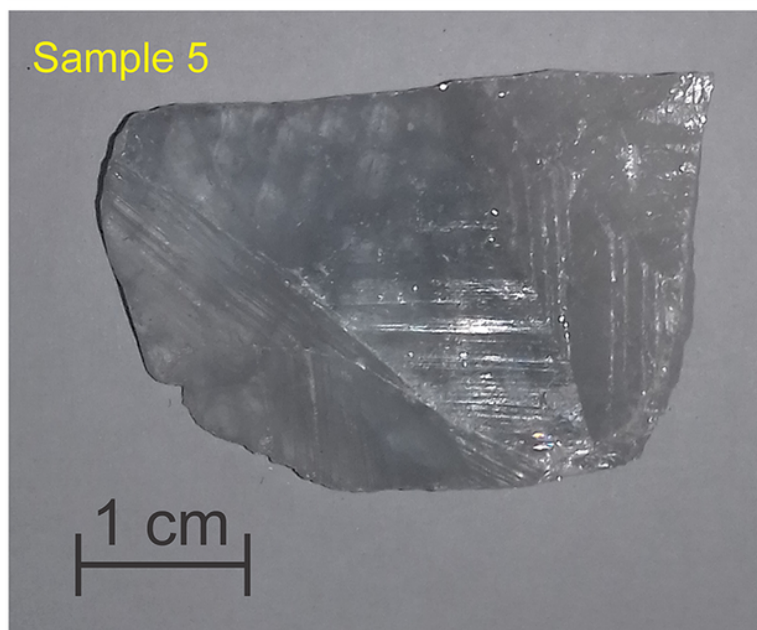


**Figure 3**

Selected 1-5 celestine samples used in the study. Photos by P. Tančić

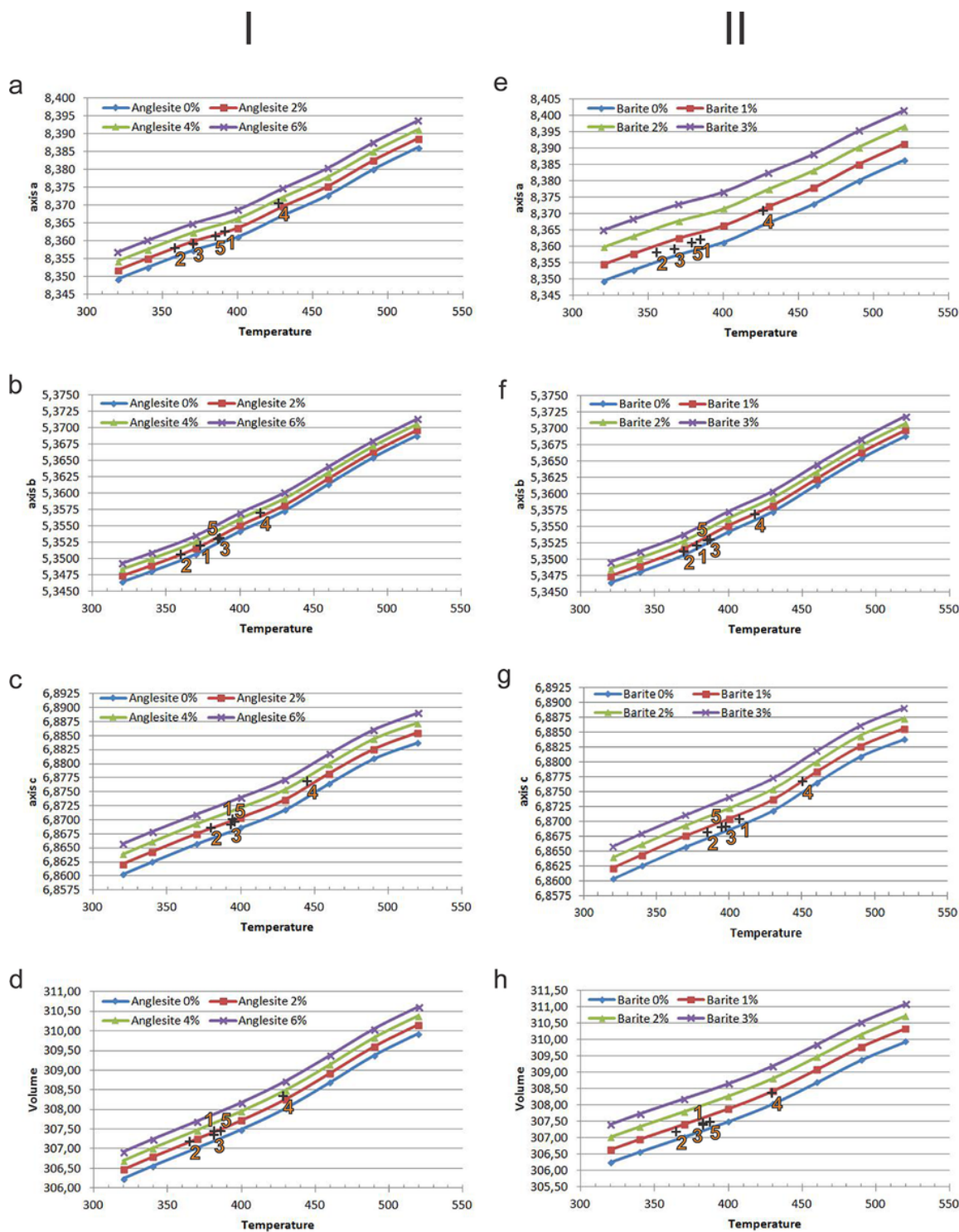


**Figure 4**

Variations of the temperature (in K) at the ambient pressure for the  $\text{Cl}_{100}\text{Ang}_0\text{-Cl}_{94}\text{Ang}_6$  (column I, left) and the  $\text{Cl}_{100}\text{Br}_0\text{-Cl}_{97}\text{Br}_3$  (column II, right) solid-solutions series (in mol. %), according to the recalculated unit-cell parameters (Tables S16 and S17 in the ESM): **a & e** axis  $a_0$  (in Å); **b & f** axis  $b_0$  (in Å); **c & g** axis  $c_0$  (in Å); and **d & h** volume  $V_0$  (in Å<sup>3</sup>)

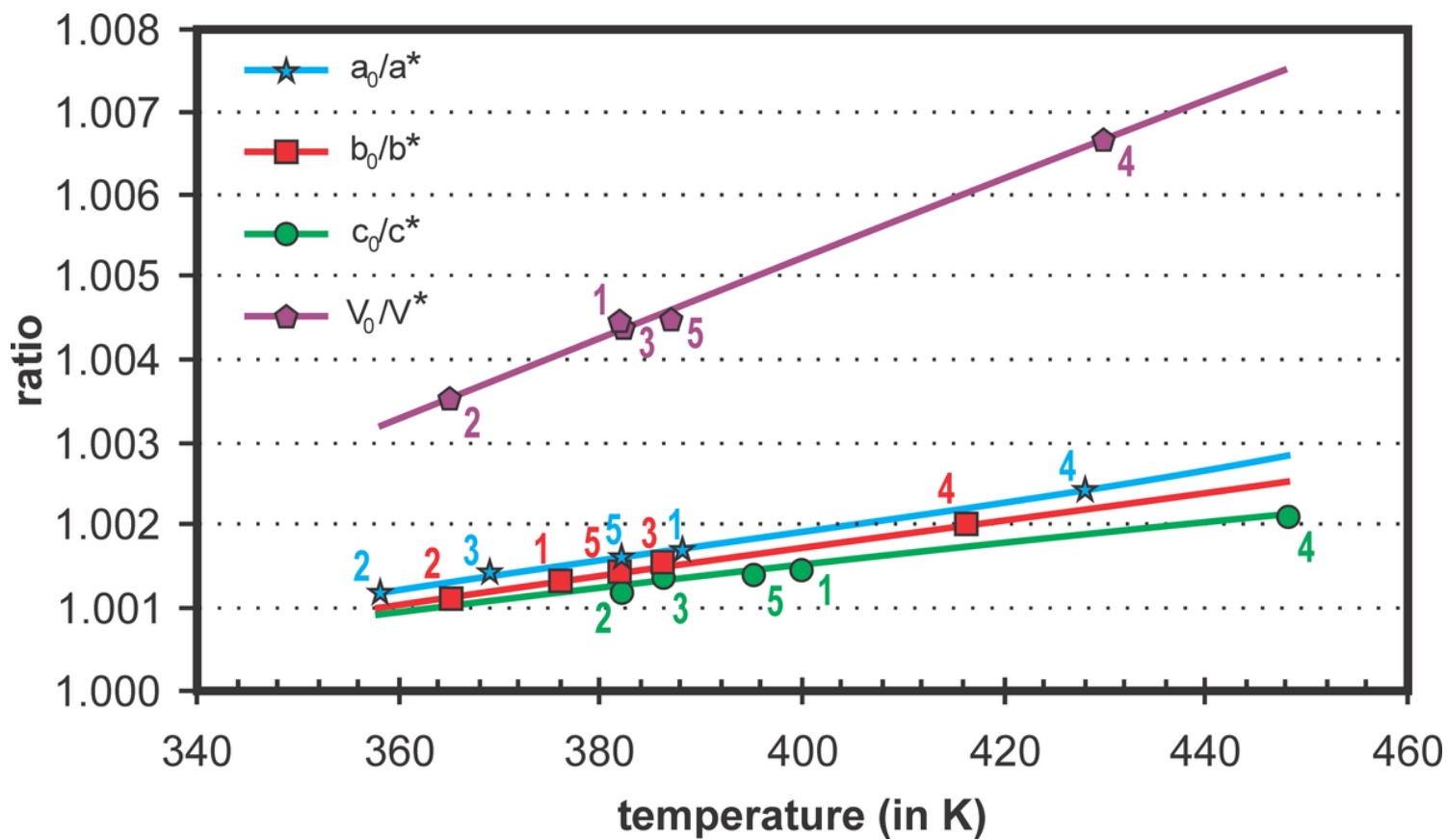


Figure 5

Temperature dependence by the relative unit-cell parameters ( $a_0/a^*$ -cyan;  $b_0/b^*$ -red;  $c_0/c^*$ -green; and  $V_0/V^*$ -purple) of the investigated 1-5 samples, at the ambient pressure conditions

## Supplementary Files

This is a list of supplementary files associated with this preprint. Click to download.

- [Supplementary.pdf](#)